



The $M \cdot \sigma_e$ relation for local type 1 AGNs and quasars

Downloaded from: <https://research.chalmers.se>, 2024-12-21 01:32 UTC

Citation for the original published paper (version of record):

Molina Tobar, J., Ho, L., Knudsen, K. (2024). The $M \cdot \sigma_e$ relation for local type 1 AGNs and quasars. *Astronomy and Astrophysics*, 691.
<http://dx.doi.org/10.1051/0004-6361/202348353>

N.B. When citing this work, cite the original published paper.

The M_{\bullet} – σ_e relation for local type 1 AGNs and quasars

J. Molina^{1,2,*}, L. C. Ho^{3,4}, and K. K. Knudsen²

¹ Instituto de Física y Astronomía, Universidad de Valparaíso, Avda. Gran Bretaña 1111, Valparaíso, Chile

² Department of Space, Earth and Environment, Chalmers University of Technology, SE-412 96 Gothenburg, Sweden

³ Kavli Institute for Astronomy and Astrophysics, Peking University, Beijing 100871, People's Republic of China

⁴ Department of Astronomy, School of Physics, Peking University, Beijing 100871, People's Republic of China

Received 23 October 2023 / Accepted 11 September 2024

ABSTRACT

We analyzed Multi Unit Spectroscopic Explorer observations of 42 local $z \lesssim 0.1$ type 1 active galactic nucleus (AGN) host galaxies taken from the Palomar-Green quasar sample and the close AGN reference survey. Our goal was to study the relation between the black hole mass (M_{\bullet}) and bulge stellar velocity dispersion (σ_e) for type 1 active galaxies. The sample spans black hole masses of $10^{6.0} - 10^{9.2} M_{\odot}$, bolometric luminosities of $10^{42.9} - 10^{46.0} \text{ erg s}^{-1}$, and Eddington ratios of 0.006–1.2. We avoided AGN emission by extracting the spectra over annular apertures. We modeled the calcium triplet stellar features and measured stellar velocity dispersions of $\sigma_{*} = 60\text{--}230 \text{ km s}^{-1}$ for the host galaxies. We find stellar velocity dispersion values in agreement with previous measurements for local ($z \lesssim 0.1$) AGN host galaxies, but slightly lower compared with those reported for nearby X-ray-selected type 2 quasars. Using a novel annular aperture correction recipe to estimate σ_e from σ_{*} that considers the bulge morphology and observation beam-smearing, we estimate flux-weighted $\sigma_e = 60\text{--}250 \text{ km s}^{-1}$. If we consider the bulge type when estimating M_{\bullet} , we find no statistical difference between the distributions of AGN hosts and the inactive galaxies on the M_{\bullet} – σ_e plane for $M_{\bullet} \lesssim 10^8 M_{\odot}$. Conversely, if we do not consider the bulge type when computing M_{\bullet} , we find that both distributions disagree. We find no correlation between the degree of offset from the M_{\bullet} – σ_e relation and Eddington ratio for $M_{\bullet} \lesssim 10^8 M_{\odot}$. The current statistics preclude firm conclusions from being drawn for the high-mass range. We argue these observations support notions that a significant fraction of the local type 1 AGNs and quasars have undermassive black holes compared with their host galaxy bulge properties.

Key words. galaxies: active

1. Introduction

The discovery of the relations between host galaxy bulge properties and the mass of central supermassive black holes (BHs; Kormendy & Richstone 1995; Magorrian et al. 1998; Ferrarese & Merritt 2000; Gebhardt et al. 2000a) has been pivotal in extragalactic astronomy during the last two decades. Nowadays, it is widely accepted that all galaxies with a massive bulge host a supermassive BH, with the BHs being a key element in regulating galaxy formation and evolution, so that the growth of both components is intimately related (Kormendy & Ho 2013, see also Greene et al. 2020). The empirical relations are key ingredients in numerical, theoretical, and semi-analytic models to reproduce the galaxy population properties (Croton et al. 2006; Schaye et al. 2015; Sijacki et al. 2015; Volonteri et al. 2016; Thomas et al. 2019; Li et al. 2020).

Among the relations between BH mass (M_{\bullet}) and host galaxy bulge properties, the BH mass–bulge mass and the BH mass–bulge velocity dispersion (σ_e)¹ correlations stand out due to their equally small scatter (~ 0.29 dex; Kormendy & Ho 2013). Several studies have attempted to find correlations with other galaxy properties (e.g., Saglia et al. 2016; de Nicola et al. 2019), but the uncertainties in the quantities prevent definitive conclusions from being reached. In all cases, the difficulty lies in measuring M_{\bullet} and σ_e for a sufficiently large galaxy population. In the very nearby universe, both quantities can be directly com-

puted. The BH masses can be measured from dynamical analysis for massive BHs (see review by Kormendy & Ho 2013), while spatially resolved galaxy spectra are needed to measure σ_e (e.g., Jørgensen et al. 1995; Cappellari et al. 2006). Beyond the nearby universe, instrumental resolution limits dynamical measurements of BH mass. We have to rely on indirect measurements that can only be applied for active galactic nucleus (AGN) host galaxies. Based on the response of the broad-line region (BLR) gas to the variable AGN continuum radiation, the reverberation mapping (RM) technique (Blandford & McKee 1982; Peterson et al. 2004; Kaspi et al. 2005; Bentz et al. 2013; Shen et al. 2015; Bentz & Manne-Nicholas 2018; Lira et al. 2018; Hu et al. 2021; Kaspi et al. 2021) has proven useful in estimating BH masses. This is possible because nearby RM AGNs follow a $M_{\bullet} - \sigma_e$ relation that is roughly parallel to that of inactive systems, offering a calibration method (Gebhardt et al. 2000b; Ferrarese et al. 2001; Nelson et al. 2004; Ho & Kim 2014). The extension of this technique, the single-epoch virial BH mass estimate (Vestergaard & Peterson 2006; Greene & Ho 2005b; Ho & Kim 2015), has allowed statistical studies of BH masses to be carried out for representative samples of the active galaxy population. The advent of high-resolution spectro-astrometric measurements with interferometry (e.g., Gravity Collaboration 2018, 2023) promises a new option for measuring M_{\bullet} in active systems.

Studying AGNs in the context of $M_{\bullet} - \sigma_e$ is still a difficult task, mainly because quantifying σ_e for such systems is challenging. Stellar velocity dispersion (σ_{*}) measurements are susceptible to the underlying stellar population properties, and their

* Corresponding author; juan.molinato@uv.cl

¹ We refer to σ_e as the stellar velocity dispersion measured inside R_e , the bulge effective radius.

relative contribution to the observed luminosity weighted galaxy spectrum. This is probably more significant for AGNs, which have complex stellar populations because of the prevalence of ongoing star formation (Jarvis et al. 2020; Shangguan et al. 2020a; Torbaniuk et al. 2021; Xie et al. 2021; Zhuang & Ho 2022; Molina et al. 2023a). In addition, the rich emission-line spectrum of type 1 AGNs blends and confuses with the stellar absorption features of the host galaxy. Moreover, the AGN continuum strongly dilutes the host galaxy spectrum. These problems are specially concerning when measuring σ_* from stellar features in the optical (Greene & Ho 2006a). Observing in the near-infrared (near-IR) is a plausible alternative (e.g., Woo et al. 2013); however, the AGN glare also limits the modeling of the stellar features at those wavelengths, even when adaptive optics-assisted observations are employed (Dasyra et al. 2007; Watson et al. 2008; Grier et al. 2013). Another option is to model narrow emission lines, such as [O III] λ 5007, to adopt the gas kinematics as a surrogate for σ_* (e.g., Nelson 2000; Shields et al. 2003). Nevertheless, those estimates are prone to large uncertainties (Nelson 2000; Onken et al. 2004; Bonning et al. 2005; Greene & Ho 2005a; Bennert et al. 2018). To avoid these important complications, the best strategy is to target the Calcium near-IR triplet (CaT) absorption lines (e.g., Ferrarese et al. 2001; Barth et al. 2002; Nelson et al. 2004; Onken et al. 2004; Greene & Ho 2006b; Woo et al. 2010) at 8498, 8542, and 8662 Å, the “gold standard” for deriving stellar velocity dispersion in active galaxies (Greene & Ho 2006a). The key advantages of using the CaT for measuring σ_* (or σ_e) is that these stellar features are largely insensitive to the underlying stellar population properties (Dressler 1984), and they are located in a spectral window that is mostly free of strong AGN emission lines. However, observing the CaT for large samples of active galaxies has been prohibitive because the absorption features can be strongly affected by sky emission, and they quickly get redshifted out of the spectral window that is accessible with optical spectrographs, only allowing σ_* to be characterized for low-redshift sources.

For this work, we used seeing-limited and ground-layer adaptive optics-aided Very Large Telescope (VLT) Multi Unit Spectroscopic Explorer (MUSE) observations to model the CaT and estimate the bulge velocity dispersion for the host galaxies of local type 1 AGNs and quasars. Our sample was built from the Palomar-Green (PG) quasar survey (Boroson & Green 1992) and the Close AGN Reference Survey (CARS; Husemann et al. 2022), with all of these at $z \lesssim 0.1$ (Figure 1). We analyzed these systems in the context of the $M_\bullet - \sigma_e$ relation, finding no difference between the active and inactive galaxies. Section 2 summarizes the properties of the active galaxy sample and outlines the observations. Section 3 details the procedures used to derive M_\bullet and σ_e . Section 4 presents the PG quasars and CARS AGNs in the context of the $M_\bullet - \sigma_e$ relation, and examines possible deviations from this relation in terms of the Eddington ratio. We discuss and summarize our findings in Section 5. Hereinafter, we refer to the central stellar spheroid component of the host galaxy simply as the “bulge”, which pertains to both classical and pseudo bulges (Kormendy & Kennicutt 2004), unless explicitly stated. We adopted a Λ CDM cosmology with $\Omega_m = 0.308$, $\Omega_\Lambda = 0.692$, and $H_0 = 67.8 \text{ km s}^{-1} \text{ Mpc}^{-1}$ (Planck Collaboration XIII 2016).

2. Sample and observations

We use VLT-MUSE wide-field-mode integral field unit (IFU) observations for our sample, which consists of 42 local

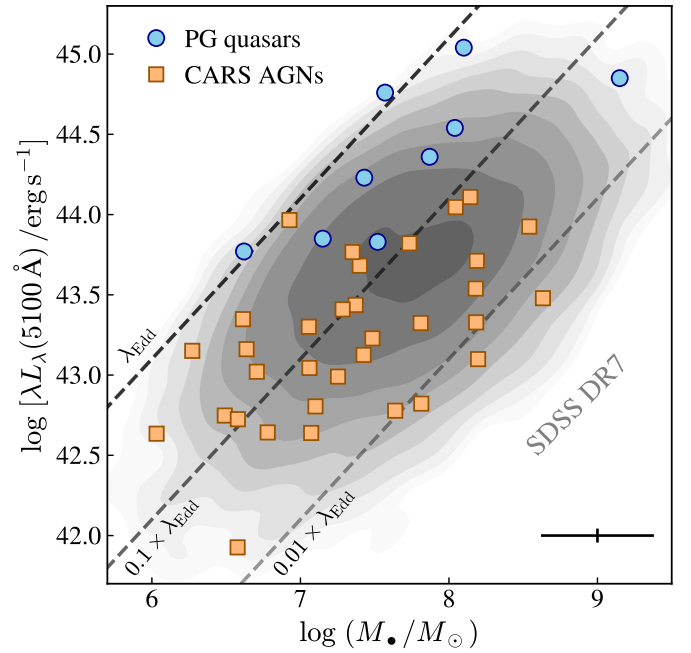


Fig. 1. AGN monochromatic luminosity at 5100 Å as a function of the BH mass. The error bar in the bottom right corner represents the typical uncertainty of the quantities. The dashed lines correspond to fixed Eddington ratios. The contours show the distribution of the broad-lined AGNs taken from the 7th data release of the Sloan Digital Sky Survey (SDSS; Abolfathi et al. 2018) at $z < 0.35$ presented by Liu et al. (2019).

($z < 0.1$; Table A.1 in Appendix A) type 1 AGNs, nine PG quasars (Boroson & Green 1992) and 33 CARS AGNs (Husemann et al. 2022). All observations were conducted as part of multiple European Southern Observatory (ESO) programs [094.B–0345(A), 095.B–0015(A), 097.B–0080(A), 099.B–0242(B), 099.B–0294(A), 0101.B–0368(B), 0103.B–0496, 0104.B–0151(A), and 106.21C7.002], spanning June 2015 to March 2021. In a single snapshot, MUSE provides a wide field-of-view of approximately $1' \times 1'$, with a $0''.2 \times 0''.2$ pixel size. It generates $\sim 90\,000$ spectra per pointing. The wavelength coverage of MUSE ranges from ~ 4700 to ~ 9350 Å, with a wavelength sampling of $1.25 \text{ Å channel}^{-1}$ at a mean resolution of $R \approx 3000$ (full width at half maximum FWHM = 2.65 Å). We analyze archival MUSE data cubes obtained from the ESO science portal². These data cubes correspond to a combination of multiple observing blocks, typically ranging from two to four per target. In the particular case of PG 0050+124, we used the “MUSE-DEEP” data cube³, which is a combination of 15 single observing blocks aimed at maximizing the signal contrast (Weilbacher et al. 2020). Most of the MUSE observations were conducted under natural-seeing conditions, with typical values $\sim 0''.5$ – $1''.4$ (Table A.2). Only four observations were assisted by the ground-layer adaptive optics module. In these cases, the MUSE spectra were masked at the 5840–5940 Å wavelength range surrounding the Na I D λ 5890, 5896 emission by the data reduction pipeline.

We further applied the Zurich Atmosphere Purge (ZAP) sky-subtraction tool (version “2.1.dev”; Soto et al. 2016) to remove residual sky features. We set CFWIDTHSP = 5, while keep-

² <http://archive.eso.org/scienceportal/home>

³ <http://www.eso.org/rm/api/v1/public/releaseDescriptions/102>

ing the other parameters at their default values. Additionally, we masked all spectra at wavelengths where strong sky-line residuals are present in the preprocessed data cubes (5578.5, 5894.6, 6301.7, 6362.5, and 7640 Å). To account for instrumental resolution, we adopt the MUSE line-spread function parameterization of Guérou et al. (2017) to correct the line widths.

2.1. PG quasars

We use the available MUSE data for nine local quasar host galaxies previously presented in Molina et al. (2022). These systems are member of the broader sample of 87 $z < 0.5$ quasars (Boroson & Green 1992) belonging to the PG survey of optical/ultraviolet color-selected quasars (Schmidt & Green 1983). These targets have substantial multiwavelength data across the entire electromagnetic spectrum, ranging from X-ray (Reeves & Turner 2000; Bianchi et al. 2009) to optical (Boroson & Green 1992; Ho & Kim 2009), mid-IR (Shi et al. 2014; Xie et al. 2021; Xie & Ho 2022), far-IR (Petric et al. 2015; Shangguan et al. 2018; Zhuang et al. 2018), mm (Shangguan et al. 2020b,a; Molina et al. 2021), and radio (Kellermann et al. 1989, 1994; Silpa et al. 2020, 2023) wavelengths. High-resolution ($\sim 0''.1$) *Hubble* Space Telescope (HST) imaging in the optical and near-IR are available for many of the host galaxies, securing accurate characterization of the host galaxy morphology (Kim et al. 2008; Zhang et al. 2016; Kim & Ho 2019; Zhao et al. 2021). Stellar masses (M_*) were computed from the multiband host galaxy images after applying the mass-to-light ratios of Bell & de Jong (2001, see Zhao et al. 2021 for more details). We estimate bolometric luminosities (L_{bol}) from the AGN monochromatic luminosity at 5100 Å, $\lambda L_{\lambda}(5100 \text{ Å})$, by adopting the conversion of Richards et al. (2006), $L_{\text{bol}} = 10 \lambda L_{\lambda}(5100 \text{ Å})$. Our PG quasar subsample is characterized by $\langle L_{\text{bol}} \rangle = 10^{45.6} \text{ erg s}^{-1}$, $\langle M_* \rangle = 10^{8.3} M_{\odot}$, $\langle M_* \rangle = 10^{10.8} M_{\odot}$, and $\langle z \rangle = 0.060$.

2.2. CARS AGNs

The CARS sample was selected from the broader Hamburg/ESO survey (HES) of ultraviolet-excess sources covering an area of $\sim 9000 \text{ deg}^2$ in the southern hemisphere. The type 1 AGNs were confirmed through follow-up spectroscopy (Wisotzki et al. 2000; Schulze et al. 2009). Specifically, CARS corresponds to a representative survey of 41 systems randomly selected from the broader subsample of 99 HES objects at $z \lesssim 0.06$ (Bertram et al. 2007). CARS probes the bright tail of the AGN luminosity function in the local universe (Schulze et al. 2009). The CARS host galaxies have been observed at multiple wavelengths, including the mm (Bertram et al. 2007) and radio (König et al. 2009). The panchromatic spectral energy distribution decomposition and stellar mass estimation for the host galaxies are presented in detail in Smirnova-Pinchukova et al. (2022). Available IFU data are presented in Husemann et al. (2022) for 41 targets, 37 of these observed by MUSE. From the MUSE dataset, we discard two targets that do not correspond to type 1 AGNs, but instead starbursts with extremely blue continuum and broad-line components tracing starburst-driven outflows (Husemann et al. 2022). Another two targets overlap with the PG quasar sample and were also discarded. Hence, we analyze 33 CARS systems (Table A.1). These CARS host galaxies are characterized by $\langle z \rangle = 0.042$, $\langle L_{\text{bol}} \rangle = 10^{44.5} \text{ erg s}^{-1}$, $\langle M_* \rangle = 10^{7.9} M_{\odot}$, and $\langle M_* \rangle = 10^{10.6} M_{\odot}$.

3. Methods

Our aim is to study local type 1 AGNs and quasars in the context of the $M_*-\sigma_e$ relation. To characterize σ_e , we focus on modeling the CaT. We minimize the effect of the AGN emission in diluting the stellar spectrum features by using annular (elliptical) apertures when extracting the spectra. For each source, we measure σ_* as close as possible to the bulge half-light radius (R_e). We develop an annular aperture correction recipe to estimate σ_e from σ_* . We further correct for systematics associated with MUSE instrumental artifacts to ensure accurate estimates. Additionally, we control for AGN emission diluting the stellar continuum and the signal-to-noise (S/N) of the stellar features.

3.1. Host galaxy spectra extraction

We begin by characterizing the projected geometry of the host galaxies on the sky. We collapse the MUSE data cubes across the spectral axis to derive “white-light” images. For each white-light image, we use the BACKGROUND2D task from PHOTUTILS (Bradley et al. 2022) to compute the background level. Then, we smooth the white-light image with a $1''$ -wide Gaussian kernel and apply DETECT_SOURCES to build a segmentation map. During this process, we mask sources with $S/N < 5$. We use the segmentation map to isolate the host galaxy from any other sources in the unsmoothed white-light image, and we apply SOURCECATALOG to derive the system position angle and ellipticity. The AGN location is assumed to coincide with the center of the host galaxy. We use the geometric parameters to construct a series of concentric annuli with thickness equal to the point-spread function (PSF) FWHM. The spectra are bounded to a window of $\pm 1000 \text{ km s}^{-1}$ to enclose the redshifted CaT⁴, with a wavelength upper limit set to 9300 Å in the observer frame to avoid the red spectral limit of MUSE. The spectra are masked whenever sky lines are present. These sky lines are identified in the corresponding variance spectra, analogously extracted from the MUSE variance data cubes. Nonetheless, we recall that the sky-line features have been minimized by applying the ZAP tool on the data cubes.

3.2. MUSE instrumental feature correction

We identify a MUSE instrumental feature at 9060–9180 Å in the observer frame (Figure 2), which must be corrected. The key characteristic of this instrumental feature is its consistent presence at the same wavelength range whenever MUSE observes a relatively bright source, such as a bright field star or the AGN. We speculate that this instrumental feature is caused by minor variations in the instrument sensitivity at specific wavelengths. We employ a “flat field-like” procedure to correct for this feature. We note that this instrumental feature overlaps with at least one CaT absorption line for AGNs at $0.046 < z < 0.080$.

We characterize the shape of the MUSE instrumental feature by using field stars (identified by *Gaia*) within the MUSE field-of-view. Out of all data cubes, we find that the spectra of 29 bright stars exhibit instrumental features. Stars are seen as point-like sources in the MUSE white-light images, so we model them using a Moffat (1969) function. We extract the stellar spectrum by spatially collapsing the data cube over a circular aperture equal to twice the Moffat model FWHM. Each stellar spectrum is fitted within the 4750–9280 Å wavelength range

⁴ For PG 1426+015 we use a window of width $\pm 1500 \text{ km s}^{-1}$ to better characterize the continuum.

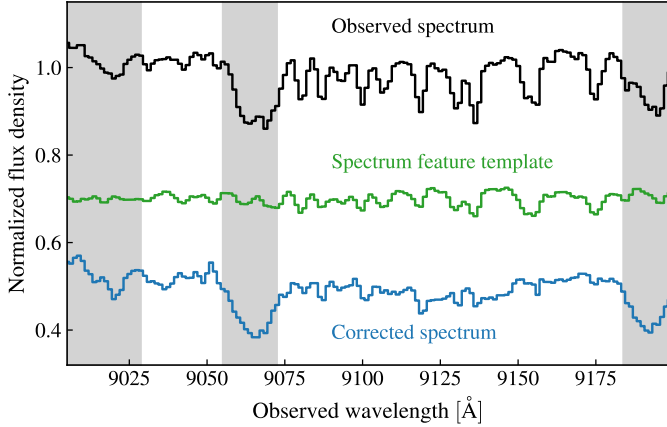


Fig. 2. Example of MUSE instrumental feature correction. The shaded regions highlight the masked wavelengths that encompass the CaT. The spectra have been vertically shifted to improve figure visualization.

using the penalized pixel-fitting (pPXF; Cappellari & Emsellem 2004) routine. We identify at least ten field stars with good-quality spectrum models, but we only use the four⁵ that deliver the best removal of the MUSE instrumental feature. We use the stellar spectra to obtain an instrumental feature template from the data minus model residuals. Then, we flux-density normalize these templates before proceeding with the MUSE instrumental feature correction. We found that the normalization value for the instrumental feature template slightly varies for each MUSE observation (see Appendix B for more details). Therefore, we determine a specific normalization value for each case. For each target, we fit the spectra extracted from all annuli over the 9030–9200 Å wavelength range using a power-law continuum model plus the instrumental feature template multiplied by a scaling factor as free parameter. During the fit, we mask a spectral window of $\pm 300 \text{ km s}^{-1}$ around each CaT absorption line, if present⁶. We compare the best-fit scaling factor with the local median spectrum flux density (computed over 9030–9200 Å), finding that the ratio between these two quantities remains approximately constant for each annulus-extracted spectrum (Figure 3). Thus, for each target, we calculate the normalization constant by averaging the ratio over all annuli-extracted spectra. Finally, we divide each annulus-extracted spectrum by its corresponding normalized instrumental feature template. Considering the ten field stars with good-quality spectrum models for building different instrumental feature templates, we estimate systematic uncertainty of 0.08 dex induced by template (star) selection.

3.3. CaT modeling and stellar velocity dispersion measurements

We employ pPXF with input stellar templates taken from the INDO-U.S. stellar spectral library of Valdes et al. (2004) to model the spectra. The stellar templates cover the 3460–9464 Å wavelength range at a uniform spectral resolution of FWHM = 1.35 Å (Beifiori et al. 2011). We use a combination of late-type (F, G, K, and M) red giant (luminosity class III) stars of near-

⁵ These stars correspond to *Gaia* DR3 3195905922532342656, 2684962933533311488, 2504238273149858816, and 2366885700060472576, which are consistent with being K-type, but were not previously selected by stellar classification.

⁶ For PG 1011–040 we use a window of width $\pm 600 \text{ km s}^{-1}$ because of the presence of calcium in emission (Persson 1988).

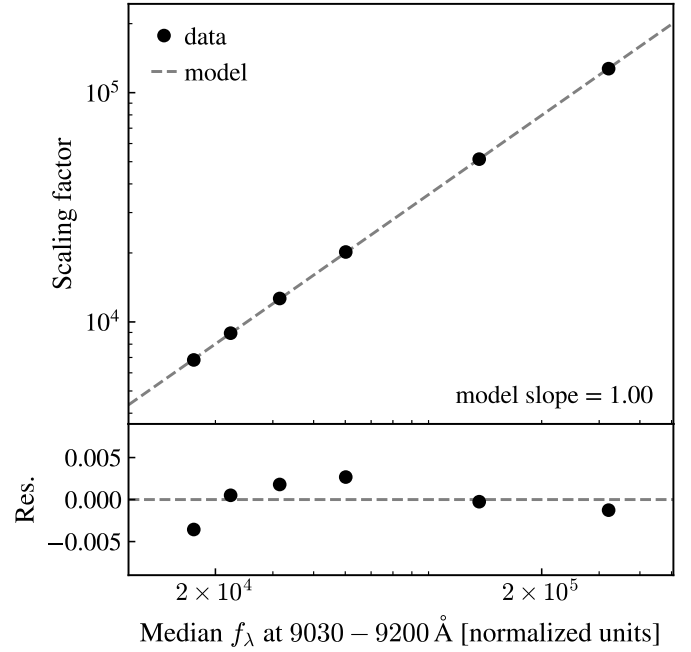


Fig. 3. Scaling factor for the instrumental feature template as a function of the median flux density for the annuli-extracted spectra over the 9030–9200 Å wavelength range (observer frame). The model corresponds to a linear function adjusted to the data. The bottom panel shows the model residuals. We only show the data for one target. We present the rest of the sample in Appendix B.

solar metallicity, plus an A-type dwarf (luminosity class V) star. We broaden the stellar templates in velocity space, taking into account their spectral resolution difference (in quadrature) with respect to the width of the MUSE line-spread function. We note that our results are not particularly sensitive to our choice of stellar template library, with an uncertainty of 0.04 dex associated with adopting other options for stellar spectral library (e.g., Vazdekis et al. 2012), or a simpler weighted linear combination of A and K stellar templates (Kong & Ho 2018). We avoid employing high-order moments (e.g., h_3 and h_4) when modeling the CaT because of the modest absorption line S/N and data spectral resolution. Even though the contrast between the AGN and its host galaxy is minimized at the CaT wavelengths, the featureless spectrum of the AGN continuum can still dominate the observed emission. The wing of the O I $\lambda 8446$ broad emission line can also interfere in the bluer end of the spectral range considered here (Caglar et al. 2020). To model such possible spectral subcomponents, we include an additive polynomial of order 0 and a multiplicative polynomial of order 3 in the pPXF setup. The inclusion of additive and multiplicative polynomials during the fit also helps to correct imperfect sky subtraction or scattered light with the former, and inaccuracies in spectral calibration or mismatches in dust reddening correction with the latter (Cappellari 2017). We caution that the inclusion of an additive polynomial tends to downweight the young (age $\lesssim 1 \text{ Gyr}$) stellar templates during the fit; however, the Ca II absorption line widths are largely insensitive to stellar population properties (Dressler 1984). Besides σ_* , deriving other parameters for the host galaxy stellar component is beyond the scope of this work.

For many of the high-luminosity AGNs the CaT lines close to the nucleus are significantly diluted by the underlying nonstellar continuum, to the extent that the stellar features are undetectable in the innermost spectrum extracted from the MUSE data cube.

Table 1. Measured and derived quantities.

Object	AGN Subtraction	R_{ap} ($''$)	EW (\AA)	S/N	σ_* (km s^{-1})	F_{ap}	σ_e (km s^{-1})	
(1)	(2)	(3)	(4)	(5)	(6)	(7)	(8)	
Palomar-Green Quasars								
PG 0050+124	Yes	1.25	1.52	0.4	9.1	177 ± 9	0.95	186 ± 22
PG 0923+129	No	2.24	1.33	2.6	19.8	152 ± 2	0.82	185 ± 22
PG 0934+013	Yes	1.44	1.47	1.2	8.5	134 ± 10	0.73	184 ± 23
PG 1011-040	Yes	1.74	2.03	2.3	9.9	136 ± 6	0.79	173 ± 23
PG 1126-041	Yes	2.07	2.48	1.4	10.0	175 ± 24	0.64	274 ± 43
PG 1211+143	Yes	1.65	2.62	0.8	11.4	65 ± 10	0.66	98 ± 19
PG 1244+026 ^(*)	Yes	1.61	1.58	1.2	12.7	80 ± 7	...	99 ± 9
PG 1426+015	Yes	1.09	1.83	0.8	4.0	208 ± 37	0.83	250 ± 53
PG 2130+099	Yes	1.76	2.21	1.4	6.8	169 ± 8	0.88	192 ± 23
CARS AGNs								
HE 0021-1810 ^(*)	No	0.60	0.65	1.8	6.1	139 ± 9	...	140 ± 9
HE 0021-1819	No	0.71	0.76	1.9	5.4	110 ± 9	1.07	103 ± 10
HE 0040-1105	No	0.85	0.73	1.7	5.9	82 ± 9	0.96	85 ± 12
HE 0108-4743	No	2.45	1.22	2.0	15.8	65 ± 2	0.99	65 ± 6
HE 0114-0015	No	1.24	1.16	2.8	7.0	129 ± 7	1.06	122 ± 10
HE 0119-0118	No	1.86	2.05	1.8	8.9	62 ± 5	1.00	62 ± 7
HE 0203-0031	No	0.76	0.65	2.2	9.8	222 ± 7	1.06	209 ± 13
HE 0212-0059	No	1.74	0.95	2.3	19.7	164 ± 3	0.88	187 ± 23
HE 0224-2834	Yes	0.89	1.06	1.3	1.3	194 ± 101	1.07	182 ± 96
HE 0227-0913 ^(*)	Yes	2.61	0.91	1.3	20.3	95 ± 3	...	96 ± 12
HE 0232-0900	Yes
HE 0253-1641	Yes	1.56	1.03	1.1	13.3	96 ± 5	1.05	91 ± 8
HE 0345+0056	Yes	1.58	1.01	0.3	14.6	80 ± 5	0.91	87 ± 11
HE 0351+0240	No	1.31	0.95	1.5	4.4	156 ± 18	0.85	183 ± 25
HE 0412-0803	Yes
HE 0429-0247	No	1.83	1.58	1.4	10.2	83 ± 5	0.79	105 ± 15
HE 0433-1028	No	1.11	0.81	0.6	3.2	99 ± 17	1.18	84 ± 16
HE 0853+0102	Yes	1.14	1.21	2.6	5.7	141 ± 9	0.92	154 ± 20
HE 0949-0122	No	2.49	1.03	1.0	13.9	97 ± 3	0.77	125 ± 16
HE 1017-0305	No	0.71	0.70	1.3	3.9	163 ± 43	1.10	148 ± 39
HE 1029-1831	No	1.32	1.09	2.0	7.6	120 ± 7	1.02	118 ± 11
HE 1107-0813	Yes	1.78	2.09	1.3	10.3	169 ± 7	0.86	196 ± 23
HE 1108-2813	No	1.68	0.84	1.9	10.5	108 ± 4	1.10	98 ± 9
HE 1237-0504	No	5.55	0.98	2.6	20.3	155 ± 2	0.91	170 ± 19
HE 1248-1356	No	1.12	0.34	1.7	12.2	88 ± 3	0.94	94 ± 10
HE 1330-1013	No	2.55	1.20	2.5	7.7	116 ± 5	1.07	108 ± 10
HE 1353-1917	No	1.45	1.04	1.1	3.3	160 ± 68	1.10	146 ± 63
HE 1417-0909	No	1.59	1.41	2.0	9.3	81 ± 6	0.99	81 ± 9
HE 2128-0221	No	1.41	1.50	2.0	5.3	60 ± 13	0.99	60 ± 14
HE 2211-3903	No	1.24	1.01	1.8	11.0	126 ± 6	1.18	106 ± 9
HE 2222-0026	No	0.47	0.55	1.6	5.7	114 ± 10	1.06	108 ± 11
HE 2233+0124	No	0.68	0.77	2.2	5.8	166 ± 11	0.96	173 ± 14
HE 2302-0857	Yes	1.29	1.23	0.8	5.7	228 ± 22	0.97	234 ± 27

Notes. (1) Source name. (2) Whether AGN emission was subtracted before obtaining σ_* (Section 3.3). (3) Aperture radius at which the stellar velocity dispersion is extracted. (4) Equivalent width of the Ca II $\lambda 8542$ feature. (5) S/N of the Ca II $\lambda 8542$ feature. (6) Stellar velocity dispersion. (7) Annular aperture correction factor. (8) Stellar velocity dispersion of the bulge. ^(*)The value of σ_e is estimated by applying the average F_{ap} value of the corresponding AGN subsample.

This allow us to consider this spectrum as an effective AGN template that can be used for modeling the AGN emission for the rest of the annuli-extracted spectra. Here, our main assumption is that the AGN is seen as a point source whose spectrum has been blurred by the MUSE PSF across the data cube. For those targets (see Table 1), we add this empirical AGN template to the pool of spectra models, but as an additional component in pPXF to avoid the AGN template broadening and shift in velocity space. For the stellar component we keep the pPXF setup as detailed above. Thus, we model the AGN emission and the CaT simultaneously. We note that the additive and multiplicative polynomials affect all the templates when using pPXF (see Equation (13) of Cappellari 2023 for more details). Figure 4 shows an example for PG 2130+099, where the AGN component is subtracted from

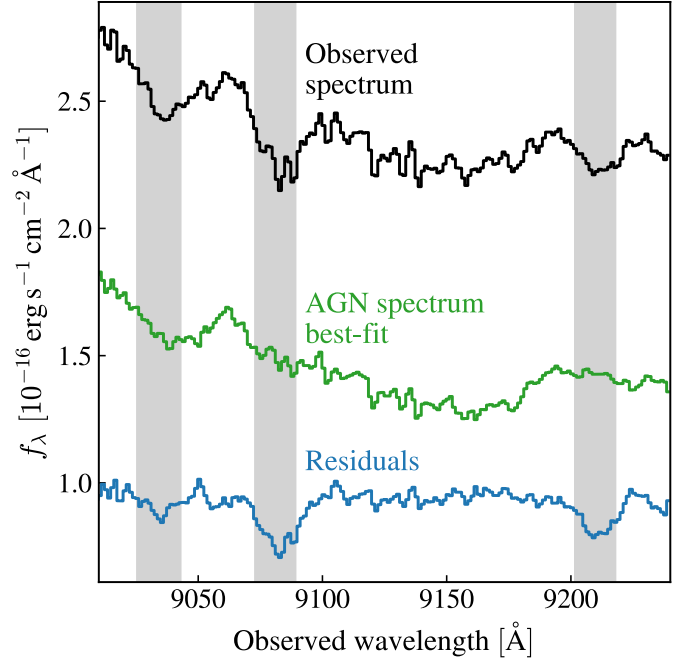


Fig. 4. Example of the AGN emission subtraction procedure. The shaded regions highlight the masked spectral windows encompassing the CaT. The AGN template has been vertically shifted to improve figure visualization. The residuals correspond to the observed spectrum minus AGN template.

the observed spectrum, and the residuals clearly show the CaT stellar features.

For each host galaxy, we select σ_* from the model spectrum taken at an aperture radius as close as possible to the bulge half-light radius, following the host galaxy bulge properties derived from HST image modeling for the PG quasars (Zhao et al. 2021) and MUSE white-light images for the CARS AGNs (Husemann et al. 2022). This radial constrain minimizes the aperture correction factor needed to convert σ_* to σ_e (see Section 3.4). For our sources, the R_e values are ~ 1 kpc on average. For the selected spectra, we also compute the equivalent width (EW) and S/N of the Ca II $\lambda 8542$ absorption line. We choose Ca II $\lambda 8542$ as reference considering that the correct modeling of this stellar feature is enough to accurately quantify σ_* from the CaT region (Harris et al. 2012). We present the selected spectra and their corresponding models in Figure A.1.

We use Monte Carlo resampling to derive the uncertainties in σ_* (Cappellari 2023). For each spectrum, the noise level (root-mean-square) is determined from the CaT model residuals. Then, we add simulated noise to the corresponding spectrum, assuming a normal distribution, and repeat the CaT fit. We iterate 1000 times to obtain a probability distribution for the best-fit parameters to estimate the 1σ uncertainties from the 16th and 84th percentiles. Table 1 provides the adopted aperture radius of the modeled spectrum and the σ_* values for each host galaxy. We emphasize that this procedure also accounts for imperfect removal of the MUSE instrumental feature (Section 3.2), which is reflected in the spectrum model residuals (e.g., see HE 0224-2834 and/or HE 2128-0221 in Figure A.1).

3.4. Stellar velocity dispersion aperture correction

For each AGN host galaxy, we use σ_* to estimate σ_e . We follow the practice of the SAURON/ATLAS^{3D} team for estimat-

Table 2. Coefficient values for computing the annuli aperture correction.

ξ	A'_{00}	A'_{01}	A'_{02}	A'_{03}	A'_{10}	A'_{11}	A'_{12}	A'_{13}	A'_{20}	A'_{21}	A'_{22}	A'_{23}
0	1.160899	0.014853	-0.002316	-0.003392	-0.125412	-0.062056	-0.082925	0.006842	0.000517	-0.007138	0.023649	-0.001860
0.25	1.113832	0.028417	0.023769	-0.004739	-0.052492	-0.077673	-0.111226	0.008231	-0.023532	0.000594	0.031723	-0.002262
0.50	1.027359	0.058682	0.060365	-0.006613	0.070241	-0.116072	-0.145055	0.009891	-0.060557	0.017315	0.040320	-0.002689
0.75	0.972627	0.077346	0.077192	-0.007407	0.135668	-0.136681	-0.150332	0.010015	-0.076557	0.026887	0.040020	-0.002632
1.00	0.943217	0.086742	0.082220	-0.007629	0.161845	-0.144046	-0.142324	0.009502	-0.079678	0.031006	0.036260	-0.002408
1.25	0.931808	0.089738	0.081267	-0.007540	0.163137	-0.142925	-0.129668	0.008746	-0.075490	0.031714	0.031682	-0.002139
1.50	0.928560	0.089947	0.078503	-0.007362	0.155299	-0.138913	-0.117671	0.008037	-0.069370	0.031187	0.027792	-0.001909
1.75	0.928987	0.089042	0.075475	-0.007175	0.144786	-0.134315	-0.107702	0.007446	-0.063277	0.030313	0.024825	-0.001732
2.00	0.930979	0.087749	0.072740	-0.007011	0.134283	-0.130023	-0.099817	0.006978	-0.057887	0.029448	0.022661	-0.001603

Notes. The parameter ξ refers to the ratio PSF FWHM/ R_e .

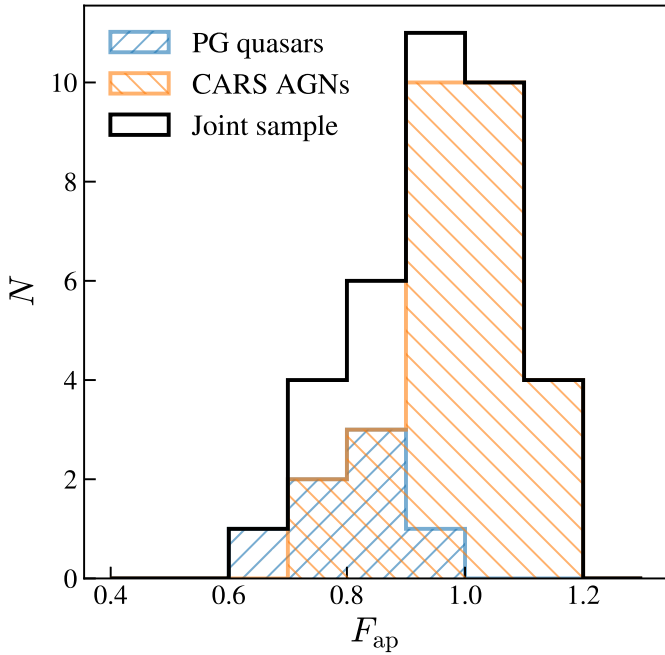


Fig. 5. Annular aperture correction factor, $F_{\text{ap}} \equiv \sigma_*/\sigma_e$, for both AGN samples.

ing σ_e , which derives the effective velocity dispersion from the luminosity weighted spectrum within R_e (e.g., Emsellem et al. 2007). The option of using spatially resolved velocity fields to derive σ_e (e.g., Gültekin et al. 2009) cannot be applied due to data limitation. However, both methods provide consistent σ_e estimates for local massive systems with classical bulges (Figure 11 of Kormendy & Ho 2013). We provide further tests showing agreement between both procedures in Appendix C).

To estimate σ_e from σ_* , we must apply an aperture correction that accounts for the radial gradient of σ_* in galaxies (Jørgensen et al. 1995; Cappellari et al. 2006). We note that the aperture correction factors provided in the literature cannot be applied to our case because they were developed for spectra extracted using circular apertures rather than annular apertures. Here, we develop a correction recipe for estimating σ_e from σ_* when using annular apertures. By assuming that the bulge surface brightness profile can be well described by a Sérsic model, an isotropic velocity dispersion (for simplicity), and a constant mass-to-light ratio, we find

$$F_{\text{ap}} = \sum_{k=0}^2 A_k(n)(R/R_e)^k, \quad (1)$$

where F_{ap} corresponds to the correction factor by which σ_* must be divided to obtain σ_e . The polynomials A_k correspond to

$$A_k(n) = A'_{k0} + A'_{k1}n^{-1} + A'_{k2}n + A'_{k3}n^2, \quad (2)$$

where the coefficients A'_{kj} depend on the central bulge stellar mass profile, modeled by the Sérsic index n . Equation (1) is flexible enough to account for the blurring effects of the MUSE PSF, parameterized in terms of the ratio $\xi = \text{PSF FWHM}/R_e$. We provide the coefficients A'_{kj} in Table 2. Equation (1) is within 2% for annular apertures located between 0.5 to $2.5 R_e$, bulge Sérsic indexes ranging from $n = 0.5$ to 8, and $\xi = 0-2.0$. This range of ξ covers the typical properties of our MUSE observations (Table A.2). Appendix D gives more details about how we derived this numerical recipe. The 1σ error for the aperture correction factor can be estimated from the uncertainties of the bulge surface brightness Sérsic profile parameters. However, these uncertainties are often underestimated due to systematics associated with non-axisymmetric components present in galaxies. Thus, we adopt a more conservative approach to compute the aperture correction factor uncertainty. For each target, we perform a Monte Carlo simulation where we vary R_e and n to compute F_{ap} using Eq. (1). The bulge half-light radius values are varied following a Gaussian distribution with width equal to the observation PSF FWHM ($0''.2$ for HST observations; Zhao et al. 2021). For the Sérsic index, we assume values varying between 0.5 and 8 with no prior information. We iterate 1000 times to obtain a probability distribution for F_{ap} and compute the 1σ error from its standard deviation. We measure a typical aperture correction factor relative uncertainty of 11% and 8% for PG quasars and CARS AGNs, respectively.

Figure 5 shows the correction factors applied to our sample, categorized into PG quasars and CARS AGNs. The annular aperture correction factors are $\sim 0.6-1.2$. On average, we find that the aperture correction factors are more significant for the PG quasar sample. This can be attributed to two factors: (1) the PG quasars tend to be at higher redshifts ($\langle z \rangle = 0.060$) compared with the CARS AGNs ($\langle z \rangle = 0.042$), resulting in spectra extracted farther away from the bulge R_e due to their smaller projected sizes on the sky; and (2) the combination of the PSF blur and high AGN luminosity in the PG quasars limiting the extraction of σ_* close to the bulge R_e . We note that the average observation seeing conditions for both AGN samples are similar ($\sim 0''.83 \pm 0''.26$).

3.5. CaT EW and S/N-associated systematics

The scattered light from the nucleus in type 1 AGNs dilutes the host galaxy stellar spectrum by a featureless continuum. This spectrum dilution leads to a decrease in the EW and S/N for

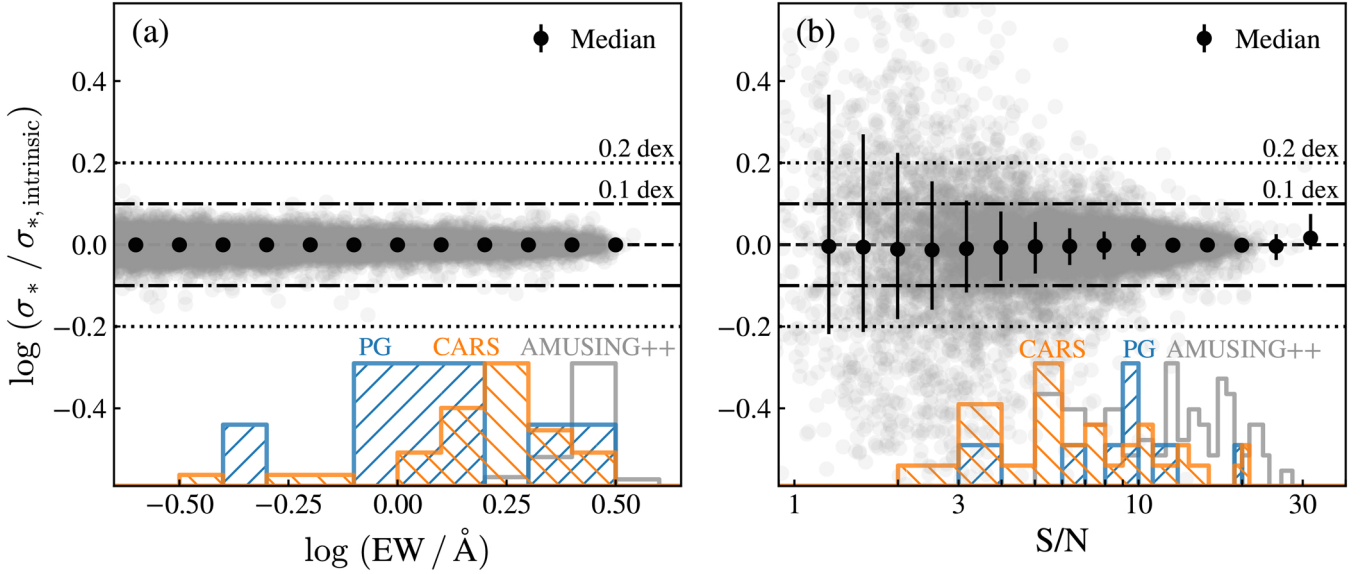


Fig. 6. Systematic uncertainty for the stellar velocity dispersion as a function of the (a) EW and (b) S/N of Ca II $\lambda 8542$. The dashed line represents the equality between the observed σ_* and the value obtained after degrading the spectra quality; dot-dashed and dotted lines represent the 0.1 and 0.2 dex scatter, respectively. At the bottom of each panel, the normalized histograms show the distribution of EW or S/N values obtained for the PG quasars, CARS AGNs, and the inactive galaxy subsample taken from the AMUSING++ survey.

the stellar features (e.g., Alexandroff et al. 2013), introducing an additional source of uncertainty when deriving σ_* . Here, we investigate the effect of the AGN dilution for our measurements.

We conduct a series of Monte Carlo simulations using MUSE observations of inactive galaxies taken from the AMUSING++ survey (López-Cobá et al. 2020). After removing Seyfert galaxies, mergers, low-quality data cubes (Ca II $\lambda 8542$ line S/N < 5), and matching the galaxies without AGN based on redshift ($0.015 < z < 0.09$), stellar mass ($10^{9.5} - 10^{11.5} M_\odot$), and star formation rate ($0.32 - 32 M_\odot \text{ yr}^{-1}$), we use 75 MUSE observations of 9 E/SO, 14 spiral, 7 peculiar, and 45 unclassified galaxies. We extracted the spectra following the procedure outlined in Section 3.1, but applying circular apertures instead of annular apertures since we do not need to consider any nuclear emission. We mimic the effects of dilution by AGN emission on the line EW by adding a constant continuum and its associated Poisson noise until the recovered Ca II $\lambda 8542$ EW reduces to 0.2 \AA . In a second test, we study the accuracy of the absorption-line width recovery against spectrum quality. This is done by adding Poisson noise to the inactive galaxy spectra until the resulting S/N of the Ca II $\lambda 8542$ line is ~ 1 . In both tests we encompass the Ca II $\lambda 8542$ line EW and S/N values measured for the type 1 AGNs presented in this work⁷. Figure 6 summarizes the results from both simulations. Although the Ca II $\lambda 8542$ line EW is significantly reduced owing to its dilution, the uncertainty of the σ_* measurements remains controlled within ~ 0.1 dex for reasonable AGN-host galaxy contrast. This is because the added Poisson noise is not high enough to critically reduce the S/N of the absorption lines. We highlight this in our second test which emphasizes the stronger link between σ_* recovery and the S/N of the stellar absorption feature. Our test results are in qualitative agreement with similar reports by Caglar et al. (2020). Note that our analysis does not include the effect of CaT being influ-

enced by blending with AGN emission lines, which are largely absent in this spectral region. The effect of CaT S/N on the uncertainty of σ_* is already considered in our Monte Carlo resampling routine.

3.6. BH mass

We estimate the BH masses following Ho & Kim (2015), who, building upon the work of Greene & Ho (2005b), present recalibrated single-epoch virial mass estimators based on the updated virial coefficients for classical bulges and pseudo bulges (Ho & Kim 2014) and the BLR size and continuum luminosity relation of Bentz et al. (2013). The BH masses (Table A.1) are computed as

$$\log M_\bullet(\text{H}\beta) = \log \left[\left(\frac{\text{FWHM}(\text{H}\beta)}{1000 \text{ km s}^{-1}} \right)^2 \left(\frac{\lambda L_\lambda(5100 \text{ \AA})}{10^{44} \text{ erg s}^{-1}} \right)^{0.533} \right] + a, \quad (3)$$

where $a = 7.03 \pm 0.02$ for classical bulges and $a = 6.62 \pm 0.04$ for pseudo bulges. The zero-point difference implies that host galaxies presenting pseudo bulges have 0.41 dex lower BH mass for fixed H β linewidth and AGN luminosity. The M_\bullet uncertainties are conservatively estimated as the sum in quadrature of the scatter of the $M_\bullet - \sigma_e$ relation used to calibrate the BH mass prescription (0.29 dex for classical bulges and ellipticals, and 0.46 dex for pseudo bulges; Ho & Kim 2014) and the scatter of the BLR-size relation (0.19 dex; Bentz et al. 2013). Thus, we adopt M_\bullet uncertainties of 0.35 dex and 0.50 dex for classical bulges and pseudo bulges, respectively. These estimates bracket the typical BH mass uncertainty of traditional single-epoch M_\bullet prescriptions (e.g., ~ 0.43 dex; Vestergaard & Peterson 2006). We classify the bulge type following Ho & Kim (2015), with classical bulges presenting $n > 2$ (but see Gao et al. 2020).

4. Results

In total, we successfully detect the CaT for 40 out of 42 host galaxies among the PG quasars and CARS AGNs. We model the

⁷ Even though spectrum quality is commonly quantified by the S/N of the stellar continuum, we prefer to use the S/N of the Ca II $\lambda 8542$ line as reference because AGN continuum subtraction is not needed for all sources (see Table 1).

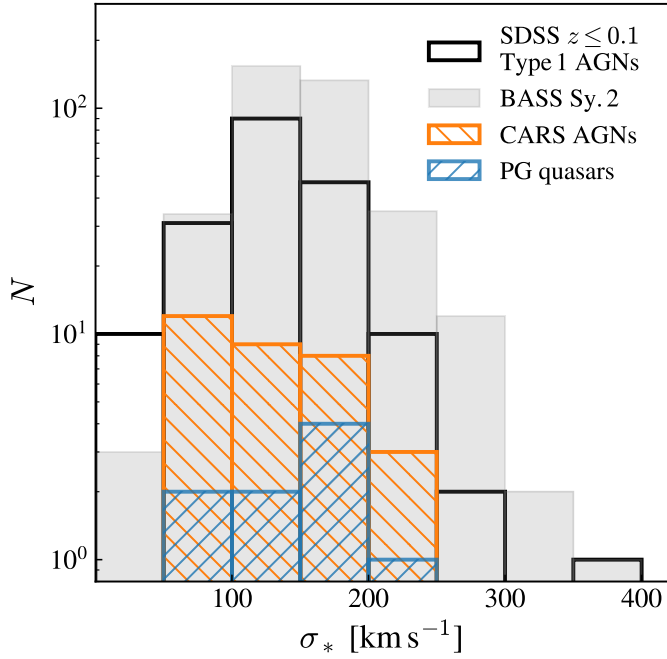


Fig. 7. Distribution of the stellar velocity dispersion for the active galaxies. Literature estimates consider SDSS $z \leq 0.1$ type 1 AGNs (Shen et al. 2008) and BASS type 2 Seyferts (including type 1.8 and 1.9 Seyferts; Koss et al. 2022b). We caution that the literature values were derived from spectra obtained using different aperture observation setups.

CaT stellar features at a median distance of $\sim 1.1 \pm 0.5$ kpc away from the host galaxy nucleus (Table 1), corresponding to ~ 0.8 times the bulge R_e . We consider the host galaxy morphology when constructing the annular apertures, minimizing the effect of host galaxy inclination when measuring σ_* . Figure A.1 provides a qualitative view for the spectral fits. Large residuals in the CaT models often correspond to sky lines that were masked during the fitting process (e.g., HE 0429–0247), and/or inaccurate removal of MUSE instrumental features (e.g., HE 0224–2834 and HE 2128–0221). The latter are considered when estimating the uncertainties for the line widths. We detect the Ca II $\lambda 8542$ line with high significance ($S/N \geq 10$) in 16 host galaxies, with low significance ($10 > S/N \geq 5$) in 18 cases, and with poor significance ($S/N < 5$) in six host galaxies. We note that systems at higher redshifts tend to have lower S/N detection. We are unable to detect the CaT in two CARS AGNs because reliable spectra extraction for the host galaxies was not possible. These host galaxies are found too compact, with the AGN radiation dominating the observed emission. After discarding targets with $S/N < 5$ detection, we obtain a total of 34 host galaxies with reliable σ_e measurements.

4.1. Stellar velocity dispersion estimates

We provide the stellar velocity measurements in Table 1. We find that σ_* values range from 60 to 230 km s^{-1} , with median values of 152 km s^{-1} for PG quasars and 116 km s^{-1} for CARS AGNs. The typical σ_* uncertainties are $\sim 10\% \pm 10\%$ ($\sim 14 \text{ km s}^{-1}$), although 8 sources have larger 1σ errors due to low-S/N detection of the CaT (e.g., HE 0224–2834, HE 1017–0305, HE 1353–1917, PG 1426+015). We note that the MUSE instrumental resolution at 9000 Å ($\sim 36 \text{ km s}^{-1}$; Guérou et al. 2017) is relatively low compared with the measured σ_* values. Veloc-

ity dispersion values close to or below the instrumental resolution may have significant scatter or be overestimated (Scott et al. 2018). For instance, Koss et al. (2022b) exclude any σ_* measurements within 20% of the instrumental resolution limit for their sample of local type 2 quasars. In our case, all of our targets are above this limit, with HE 2018–0221 presenting the lower σ_* value, 67% higher than the MUSE spectral resolution.

From the literature, we find few σ_* measurements for our targets that can be used to make rough comparisons. Here, we report any σ_* measurement irrespective of the stellar feature observed. Dasyra et al. (2007) presented near-IR H -band spectra modeling (mainly using CO stellar features; their Figure 2) for PG 0050+124 ($\sigma_* = 188 \pm 36 \text{ km s}^{-1}$), PG 1126–041 ($\sigma_* = 194 \pm 29 \text{ km s}^{-1}$), PG 1426+015 ($\sigma_* = 185 \pm 67 \text{ km s}^{-1}$), and PG 2130+099 ($\sigma_* = 156 \pm 18 \text{ km s}^{-1}$). Those spectra were obtained by using slits with widths of $\sim 1''.0 - 1''.4$, but avoiding the nuclear zones ($\leq 0''.3 - 0''.4$). Grier et al. (2013) presented adaptive optics-assisted Gemini near-IR IFU measurements, also taken in the H -band, for PG 1426+015 ($\sigma_* = 211 \pm 15 \text{ km s}^{-1}$) and PG 2130+099 ($\sigma_* = 167 \pm 19 \text{ km s}^{-1}$). Those measurements were extracted over annular apertures avoiding the AGN emission; they set annulus inner radius $\sim 0''.2 - 0''.4$ and outer radius $\sim 0''.6 - 1''.7$. Bennert et al. (2011) use Keck/LRIS long-slit spectroscopy to isolate the host galaxy emission and measure σ_* for HE 0203–0031 and HE 0119–0118. Based on CaT modeling and apertures equal to the bulge R_e , they report $\sigma_* = 200 \pm 9 \text{ km s}^{-1}$ and $89 \pm 10 \text{ km s}^{-1}$, respectively. Busch et al. (2015) targeted HE 1029–1931 with seeing-limited SINFONI observations in the K band, reporting $\sigma_* = 104 \pm 20 \text{ km s}^{-1}$, using an aperture $\sim 0''.6$. Finally, for HE 1237–0504, Caglar et al. (2020) estimate $\sigma_* = 145 \pm 4 \text{ km s}^{-1}$ by modeling the CO(2–0) absorption features observed with SINFONI (adaptive optics-assisted). Although different procedures and modeled stellar features make direct comparisons difficult, all of these literature measurements of σ_* are consistent with ours (Table 1). Using the adaptive optics observations as the main reference for duplicate literature values, we find a mean σ_* ratio (literature divided by ours) of 1.04 with a standard deviation of 0.17.

Figure 7 shows the distribution for our σ_* measurements. In contrast with the PG quasars, for the CARS sample we find more systems with $\sigma_* \leq 150 \text{ km s}^{-1}$, which is consistent with the CARS survey covering less luminous AGNs with less massive BHs in less massive host galaxies and at lower redshifts (Section 2). Additionally, we compare with the σ_* distributions for two other AGN samples: local $z \leq 0.1$ type 1 AGNs (Shen et al. 2008) from the SDSS and type 2 AGNs from the BAT AGN Spectroscopic Survey (BASS; Koss et al. 2022a). We only select the BASS type 2 AGNs with CaT-based σ_* values, corresponding to host galaxies at $z \leq 0.065$ (Koss et al. 2022b). Both samples provide a broader reference for type 1 AGNs, but it should be noted that their measurements may be less precise than ours for classical bulges and pseudo bulges because of aperture effects. For example, the SDSS data were obtained using $3''$ -wide fibers. Despite this limitation, the BASS and SDSS samples still serve as a valuable comparison, especially considering the small correction needed for aperture effects. In the joint sample of PG quasar and CARS AGN host galaxies, we find a range of σ_* values similar to those estimated for the SDSS $z \leq 0.1$ sample. The BASS type 2 AGNs tend to present a higher fraction of host galaxies with larger σ_* . This type 1-type 2 AGN dichotomy has been already noted by Koss et al. (2022b), and can be linked to the differences in the properties of their host galaxies, with the type 2 AGN host galaxies likely being more massive (see also Koss et al. 2011).

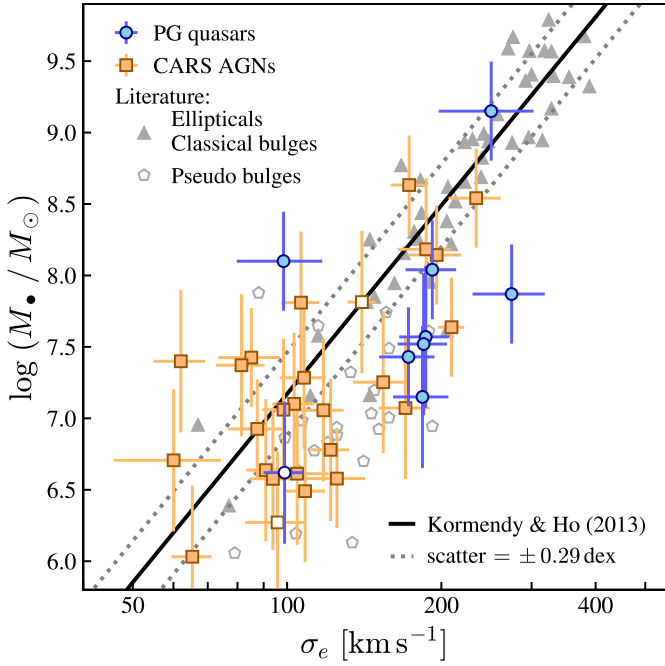


Fig. 8. $M_{\bullet} - \sigma_e$ relation for local type 1 AGNs and inactive galaxies. Colored open circles correspond to three AGNs for which the median sample aperture correction factor was adopted to estimate σ_e . The data for inactive galaxies are taken from Kormendy & Ho (2013), as well as the best-fit relation (their Equation (7)) and scatter.

After applying the aperture correction factors (Figure 5), we report σ_e values in the range of 60–250 km s⁻¹, with median values of 185 km s⁻¹ for the PG quasars and 108 km s⁻¹ for the CARS sample. The typical σ_e uncertainties $\sim 16\% \pm 6\%$ ($\lesssim 25$ km s⁻¹).

4.2. The $M_{\bullet} - \sigma_e$ relation

Figure 8 shows the relation between BH mass and σ_e for the active galaxies. We primarily sample the parameter space at $M_{\bullet} \lesssim 10^8 M_{\odot}$, where we detect a large scatter (~ 0.6 dex) when considering the relation of Kormendy & Ho (2013) as reference. The CARS AGNs mainly span $M_{\bullet} - \sigma_e$ at $M_{\bullet} \lesssim 10^{7.5} M_{\odot}$, while the PG quasars complement CARS for higher BH masses. The lack of AGN data at higher BH masses is mainly due to the redshift upper limit for our sample ($z \lesssim 0.1$). By performing a multivariate Cramér test (Baringhaus & Franz 2004), using the Kormendy & Ho (2013) sample as reference for $M_{\bullet} \lesssim 10^8 M_{\odot}$, we find no difference between the active and inactive galaxy samples (p -value = 0.69). The p -value decreases to 0.42 when considering a BH mass upper limit of $10^{8.5} M_{\odot}$, but this is largely due to poor AGN sample statistics at $M_{\bullet} \gtrsim 10^8 M_{\odot}$.

Our BH mass estimates rely on the BLR size-luminosity relation of Bentz et al. (2013). Woo et al. (2024) recently suggested a slightly shallower trend for this relation. They report typical BLR sizes being smaller for the more luminous AGNs [$\lambda L_{\lambda}(5100 \text{ \AA}) \gtrsim 10^{44} \text{ erg s}^{-1}$], suggesting less massive BHs because M_{\bullet} scales linearly with BLR size. We explore this possibility by reestimating the BH masses following the BLR size-luminosity relation of Woo et al. (2024) and Ho & Kim (2015). For AGNs with $\lambda L_{\lambda}(5100 \text{ \AA}) \gtrsim 10^{44} \text{ erg s}^{-1}$ (eight systems; six PG quasars) the BH masses decrease by $\gtrsim 0.15$ dex. HE 1248–1356 is the only system for which the

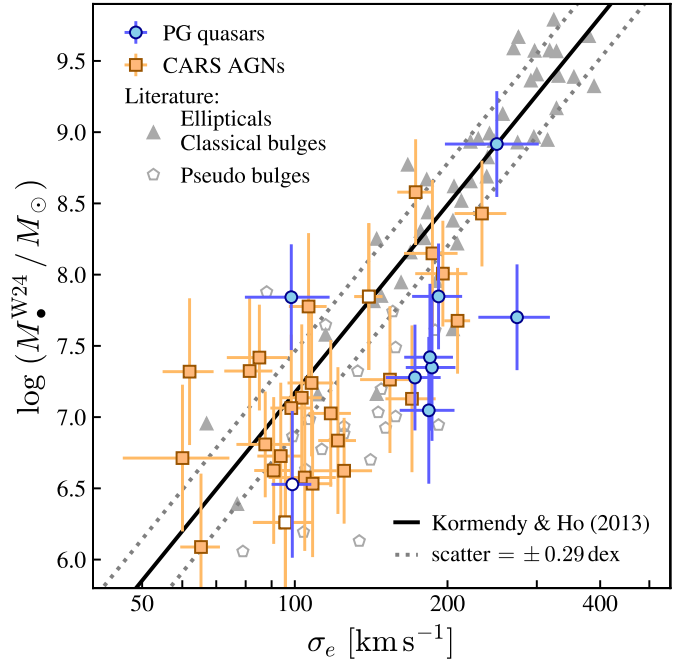


Fig. 9. $M_{\bullet} - \sigma_e$ relation for local type 1 AGNs, as in Figure 8, but updating the BH mass estimates following the BLR size-luminosity relation of Woo et al. (2024).

BH mass increases by $\gtrsim 0.15$ dex due to its low AGN luminosity [$\lambda L_{\lambda}(5100 \text{ \AA}) \lesssim 10^{42} \text{ erg s}^{-1}$]. For all other AGNs, the BH masses vary by $\lesssim 0.15$ dex, well below the typical M_{\bullet} uncertainty range. Figure 9 presents our sample with updated BH masses (M_{\bullet}^{W24}). A multivariate Cramér test suggest no difference between the active and inactive galaxy samples (p -value = 0.49), in agreement with our previous report.

Considering the 1σ lower limit of the $M_{\bullet} - \sigma_e$ relation (0.29 dex scatter) and the 1σ uncertainties of our M_{\bullet} and σ_e estimates, Figure 8 suggests four out of eight PG quasars and five out of 26 CARS AGNs lie below the $M_{\bullet} - \sigma_e$ relationship for ellipticals and classical bulges (Kormendy & Ho 2013), largely following the galaxies with pseudo bulges (Saglia et al. 2016). Finding some systems below $M_{\bullet} - \sigma_e$ might not be surprising, as we adopted the single-epoch BH mass prescription of Ho & Kim (2015), which systematically offsets the systems with pseudo bulge -0.41 dex below the classical $M_{\bullet} - \sigma_e$ relation. To check whether this assumption drives our results, in Figure 10 we show $M_{\bullet} - \sigma_e$ differentiated by bulge type. For pseudo bulges, we adopt the best-fit reported by Ho & Kim (2014, ~ 0.46 dex scatter). They modeled the data collated in Kormendy & Ho (2013) keeping the slope fixed to that of the $M_{\bullet} - \sigma_e$ relation of classical bulges and ellipticals during the fitting process. We find that five out of nine of the AGN hosts located below $M_{\bullet} - \sigma_e$ for classical bulges and ellipticals are systems with pseudo bulges, suggesting that the adopted BH mass prescription may be effectively producing such trend. However, we report four AGN hosts with classical bulges below $M_{\bullet} - \sigma_e$ (e.g., HE 0949–0122, PG 2130+099). Literature data also show some systems with classical bulges following such trend. These AGN hosts are immune to the BH mass systematic described above. For example, by adopting the BH mass prescription of Vestergaard & Peterson (2006), which does not differentiate AGN host galaxies by bulge type, to reestimate M_{\bullet} , all the systems with pseudo bulges shift upward in the

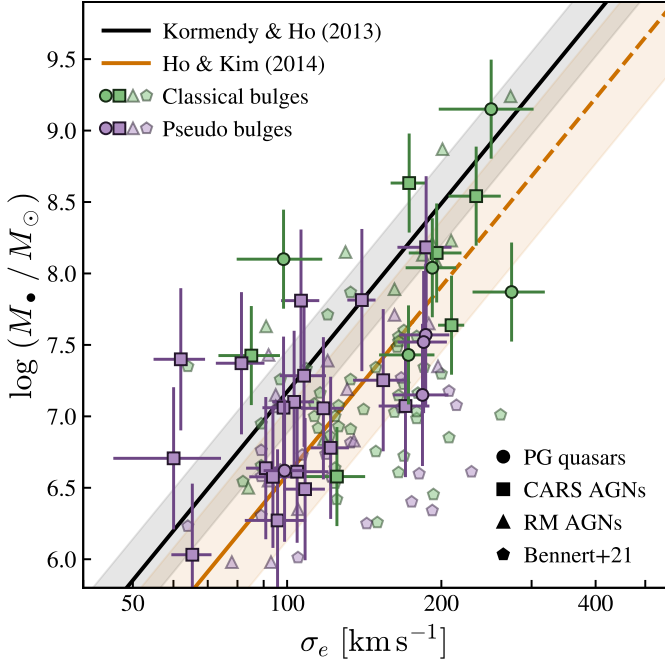


Fig. 10. M_{\bullet} – σ_e relation for local type 1 AGNs, as in Figure 8, highlighting the best-fit relations for classical bulges (Kormendy & Ho 2013) and pseudo bulges (Ho & Kim 2014). We differentiate the systems by bulge type. The shaded regions represent the intrinsic scatter for both relations, 0.29 dex and 0.46 dex, respectively. The dashed line indicates the extrapolation of the best-fit relation for pseudo bulges at high BH masses. We also show the RM AGNs presented in Ho & Kim (2014, 2015) and the local AGN sample of Bennert et al. (2021).

M_{\bullet} – σ_e plane (Figure 11), as expected. Only two AGN hosts with pseudo bulge remain below the M_{\bullet} – σ_e relation for classical bulges and ellipticals after considering their BH mass uncertainty (0.43 dex; Vestergaard & Peterson 2006). However, the four AGN host galaxies with classical bulges continue to line below the M_{\bullet} – σ_e relation. We observe similar trends for the literature data. We note that a multivariate Cramér test indicates that our sample does not differ from that of inactive galaxies taken from Kormendy & Ho (2013, p -value < 0.01) after adopting the BH mass prescription of Vestergaard & Peterson (2006).

Figure 8 also shows two systems lying above the M_{\bullet} – σ_e relation, HE 0119–0118 and PG 1211+143. When looking carefully, we find that HE 0119–0118 has a barred host galaxy (Husemann et al. 2022), and PG 1211+143 is compact (Zhao et al. 2021). It is well-known that measuring bulge properties in barred galaxies is difficult (Gao & Ho 2017, and references therein). We conjecture similar issues for PG 1211+143, where the host galaxy morphology and AGN emission critically undermine accurate host galaxy image decomposition. Therefore, we cannot be certain of the accuracy of the offset with respect to M_{\bullet} – σ_e for these two systems. It is possible that those measurements also reflect biased estimations of σ_e due to poor host galaxy bulge characterization, in cases where the bulge is too compact and the region from where we extract σ_* corresponds to that of a bar or disk. We caution that the results presented in this section depend, in part, on the adopted M_{\bullet} scaling relationship (e.g., Shankar et al. 2019) and the criteria used to classify bulge type.

Another source of uncertainty arises from estimating σ_e (and σ_*) itself. We have estimated σ_e from a spectrum obtained by collapsing the host galaxy emission over an

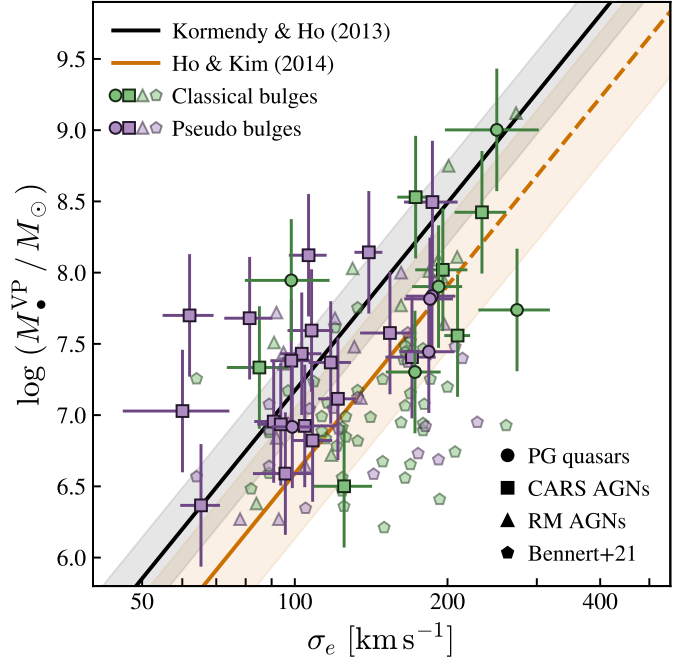


Fig. 11. M_{\bullet} – σ_e relation for local type 1 AGNs, as in Figure 10, but adopting the single-epoch BH mass prescription of Vestergaard & Peterson (2006). The M_{\bullet} uncertainty is 0.43 dex.

aperture. This method differs from that usually employed in observations that spatially resolve the galaxy kinematics (e.g., Gültekin et al. 2009; Kormendy & Ho 2013). Differential rotation, which is minimized by analyzing kinematic fields, may artificially broaden the spectrum obtained from an aperture, effectively increasing the estimated σ_e . While this effect may be minor for bulges, it may be significant for pseudo bulges due to their higher rotation support. Greene & Ho (2005a) suggest that rotational broadening may be small. Bennert et al. (2011) find an average increase $\sim 10\%$ for σ_e due to rotational broadening, but they note that rotational broadening could be more significant for edge-on systems (up to $\sim 40\%$, implying ~ 0.6 dex difference in BH mass offset). Note that, in the context of elliptical galaxies σ_e is computed by co-adding spectra within apertures (e.g., Cappellari et al. 2006) even though they also typically rotate (Cappellari 2016). We emphasize that we are comparing our sample with the inactive galaxy sample of Kormendy & Ho (2013), whose σ_e measurements were obtained from spatially resolved kinematics. Kormendy & Ho (2013) compared their estimates with aperture-based values provided by the SAURON/ATLAS^{3D} team for massive galaxies with classical bulges, and found no major discrepancies (see their Figure 11b). We test the consistency of both procedures for systems with bulge and pseudo bulges by analyzing mock data in Appendix C. The mock data are built with galaxy properties encompassing those of our targets (Tables A.1 and 1). We find good agreement between both methods in estimating σ_e , with aperture-based values overestimating those obtained from spatially resolved kinematic maps by $\sim 2\% \pm 2\%$ for $\sigma_e \geq 75 \text{ km s}^{-1}$. However, we caution that our test suggests a significant overestimation of σ_e by the aperture-based method when the linewidths of the absorption features are comparable to the spectral resolution of the observations (see Appendix C, for more details).

One remaining uncertainty is whether to account for inclination effects when computing σ_e . Bennert et al. (2015) show that correcting σ_e for inclination may increase the values by up to

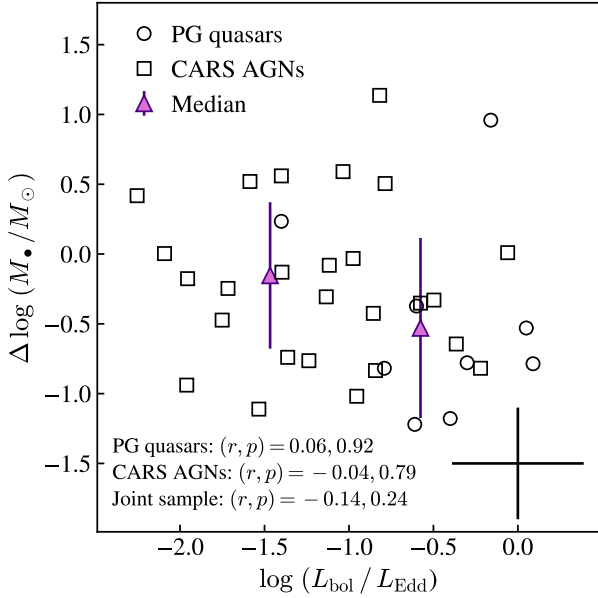


Fig. 12. BH mass offset from the $M_{\bullet} - \sigma_e$ relation of Kormendy & Ho (2013, their Equation (7)) as a function of the Eddington ratio. The error bars in the bottom right corner represent the BH mass and Eddington ratio 1σ uncertainties. We detail the correlation coefficient r and p -value for the PG quasars, CARS AGNs, and the joint sample.

$\sim 40\%$. However, as Bennert et al. (2015) note, not correcting σ_e for inclination is the common practice in the literature, meaning that any potential systematic bias would affect all galaxy samples, not just those hosting AGNs. Nevertheless, we find no correlation between BH mass offset from the $M_{\bullet} - \sigma_e$ relation and galaxy inclination for our sample.

4.3. Deviations from the $M_{\bullet} - \sigma_e$ relation

Literature studies suggest that active galaxies with more efficiently accreting BHs tend to deviate from $M_{\bullet} - \sigma_e$, with the Eddington ratio⁸ being inversely correlated with the BH mass offset (e.g., Shen et al. 2008; Ho & Kim 2014). The CARS AGNs and the PG quasars contain local AGNs with high $L_{\text{bol}}/L_{\text{Edd}}$, making our sample ideal for testing departures from the $M_{\bullet} - \sigma_e$ relation. The PG quasars mainly sample $L_{\text{bol}}/L_{\text{Edd}} \gtrsim 0.1$, while the CARS AGNs are spread all over the range $L_{\text{bol}}/L_{\text{Edd}} = 0.01 - 1$, although the majority of these systems present $L_{\text{bol}}/L_{\text{Edd}} \lesssim 0.1$. We compute the BH mass offset from $M_{\bullet} - \sigma_e$, using as reference Equation (7) of Kormendy & Ho (2013):

$$\Delta \log (M_{\bullet}/M_{\odot}) = \log \left(\frac{M_{\bullet}}{M_{\odot}} \right) - 4.38 \log \left(\frac{\sigma_e}{200 \text{ km s}^{-1}} \right) + 8.49. \quad (4)$$

Figure 12 shows the BH mass offset as a function of Eddington ratio. We find no clear trends. Dividing the data into two bins of Eddington ratio, AGNs with $L_{\text{bol}}/L_{\text{Edd}} \leq 0.1$ present a median M_{\bullet} offset of -0.15 , with a scatter of 0.52 dex. Objects with $L_{\text{bol}}/L_{\text{Edd}} > 0.1$ show a median BH mass departure equal to -0.53 , with a scatter of 0.65 dex. We compute Kendall τ correlation coefficients for both AGN samples and the joint sample (PG quasars plus CARS AGNs). In this analysis, we include the 1σ uncertainties of the quantities involved. We

⁸ We compute the Eddington ratio as $L_{\text{bol}}/L_{\text{Edd}}$, where $L_{\text{Edd}} = 1.26 \times 10^{38} (M_{\bullet}/M_{\odot}) \text{ erg s}^{-1}$.

consider a correlation to be valid only if the probability of it occurring by chance is ≤ 0.05 . For the PG quasars, we compute $r = 0.06_{-0.22}^{+0.22}$ with a p -value of 0.92, while for the CARS AGNs we estimate $r = -0.04_{-0.10}^{+0.09}$ with a p -value of 0.79. For the joint sample, we compute $r = -0.14_{-0.08}^{+0.08}$ with a p -value of 0.24. No statistically significant correlation is seen. We find similar results when only considering host galaxies with CaT $S/N > 10$. Bearing in mind that galaxies with pseudo bulges are offset from $M_{\bullet} - \sigma_e$ and exhibit larger scatter (Kormendy & Ho 2013), we further distinguish host galaxies with classical or pseudo bulges. Figure 13 presents the data color-coded by bulge type, with the classical bulges labeled following two common classification schemes: the traditional Sérsic index > 2 threshold (Kormendy & Kennicutt 2004; Fisher & Drory 2008), and $B/T > 0.1$ (Gao et al. 2020; Quilley & de Lapparent 2023). For the first case, we find no correlation for either bulge type (classical bulges: $r = -0.13_{-0.15}^{+0.18}$, $p = 0.65$; pseudo bulges: $r = -0.15_{-0.11}^{+0.11}$, $p = 0.31$). For the second case, the limited statistics preclude us from computing a correlation coefficient for pseudo bulges. For galaxies hosting classical bulges, we find no significant correlation ($r = -0.16_{-0.09}^{+0.10}$, $p = 0.22$) after correcting L_{Edd} , M_{\bullet} , and BH mass offset considering our adopted bulge-type dependent BH mass prescription (Ho & Kim 2015). However, we caution that using the B/T ratio for classifying bulge type in AGN host galaxies is highly misleading, as it is known that the central spheroid can be overluminous from recent star formation activity (Kim & Ho 2019). Furthermore, bulge model uncertainties are pernicious in the presence of a bright AGN glare. While we have some confidence in the AGN-host decomposition of the PG quasars, which were based on HST images (Zhao et al. 2021), the image analysis of the CARS AGNs was limited to MUSE white-light images (Husemann et al. 2022). We lack the statistics necessary to study subtle trends with respect to host galaxy morphology.

We complement our sample by including the less-luminous RM AGNs presented in Ho & Kim (2014, 2015) and the local AGNs observed by Bennert et al. (2021, Figure 14). When combining the three data sets, the correlation coefficient slightly reduces to $r = -0.12_{-0.05}^{+0.05}$ with a p -value of 0.05. However, we note that the low p -value is mainly driven by the AGNs with Eddington ratio < 0.01 (only four objects). By excluding these AGN hosts we obtain $r = -0.09_{-0.05}^{+0.04}$ and $p = 0.15$. The p -value is not low enough to imply a significant inverse correlation between BH mass offset and $L_{\text{bol}}/L_{\text{Edd}}$.

5. Discussion and summary

Early studies commonly reported that the AGN host galaxies tend to follow a different $M_{\bullet} - \sigma_e$ relation compared with that of inactive galaxies (e.g., Greene & Ho 2006a; Shen et al. 2008; Ho & Kim 2014). This was interpreted as a natural consequence of bright AGNs being preferentially hosted in late-type galaxies, considering that these systems tend to present pseudo bulges (Kormendy & Kennicutt 2004) and pseudo bulge hosts lie below the $M_{\bullet} - \sigma_e$ relation of classical bulges and ellipticals (Hu 2008; Greene et al. 2010; Kormendy & Ho 2013; Saglia et al. 2016; de Nicola et al. 2019). However, opposite reports have also been presented (e.g., Nelson et al. 2004; Woo et al. 2010, 2013; Bennert et al. 2011, 2015; Caglar et al. 2020). By analyzing spatially resolved σ_* profile data, Bennert et al. (2021) suggest that AGN host galaxies with a pseudo bulge follow the $M_{\bullet} - \sigma_e$ relation of classical bulges and ellipticals. Our measure-

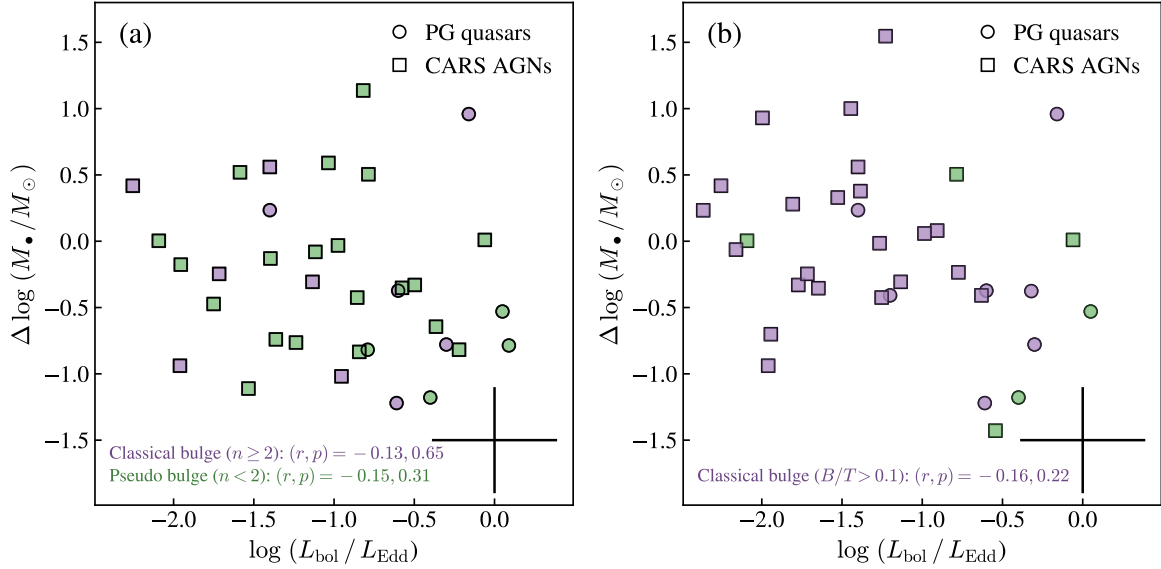


Fig. 13. Similar to Figure 12, but color-coding the data by the host galaxy bulge type, which is differentiated by (a) Sérsic index n and (b) the B/T ratio. We correct the BH mass-related quantities according to the bulge-type classification following the BH mass prescription of Ho & Kim (2015).

ments for the type 1 AGNs and quasars agree with the classical bulge–pseudo bulge dichotomy for $M_{\bullet} - \sigma_e$. Many of the PG quasars are located below the relation of Kormendy & Ho (2013) for classical bulges, in the regime of pseudo bulges, even though their central spheroids are classical bulges. Similar systems are also present in the sample of Bennert et al. (2021, Figure 10). It is unlikely that underestimated BH masses is the sole cause in producing such trends. We have used the BH mass prescription of Ho & Kim (2015), which was explicitly calibrated for RM AGNs (Ho & Kim 2014) using the $M_{\bullet} - \sigma_e$ relation of inactive galaxies (Kormendy & Ho 2013). The difference in zero-point applied for host galaxies with classical bulges and pseudo bulges (Equation 3) can only account for a M_{\bullet} offset up to 0.41 dex for systems with a pseudo bulge. Still some AGN hosts with a pseudo bulge deviate ≥ 1 dex from $M_{\bullet} - \sigma_e$ (Figure 13a). However, we find average BH mass offsets from $M_{\bullet} - \sigma_e$ of $\sim -0.25 \pm 0.18$ dex for AGN hosts with a classical bulge and -0.31 ± 0.11 dex for those with a pseudo bulge, implying that any claim is on weak grounds. If we adopt the traditional single-epoch BH mass prescription of Vestergaard & Peterson (2006), which does not distinguish by bulge type, many of the AGN hosts with a pseudo bulge shift upward, closer to $M_{\bullet} - \sigma_e$. Only a minor fraction (16%) of AGN hosts remain below $M_{\bullet} - \sigma_e$ (Figure 11). However, in such a case, our AGN sample distribution on the $M_{\bullet} - \sigma_e$ plane would become significantly different from that of inactive galaxies taken from Kormendy & Ho (2013, multivariate Cramér test p -value < 0.01). It is unclear why both samples may depart from each other, such that most of the disk-like AGN hosts may present overmassive BHs (or pseudo bulges with a lower σ_e) compared with the inactive spirals. BH masses could be underestimated if the BLR has a significant amount of dust, with ~ 0.3 – 0.4 dex offsets reported for less luminous AGNs (Caglar et al. 2020). However, such BH mass offsets are not enough to explain our data, as mentioned above. Adopting the recent BLR-size luminosity relation of Woo et al. (2024) instead of that of Bentz et al. (2013) strengthens our finding, as Woo et al. (2024)’s BLR-size relation suggests less massive BHs for the more luminous AGNs. We note that the CaT is largely insensitive to the underlying stellar population properties

(Dressler 1984), suggesting that our findings should be robust against recent star formation activity that might induce systematic bias in AGN hosts. These findings are consistent with reports on active galaxies in the context of the BH mass–bulge mass relation, where some active galaxies have a systematically lower M_{\bullet} than inactive galaxies for both cases when (Molina et al. 2023a) or when not differentiating (Kim et al. 2008; Zhao et al. 2021; Ding et al. 2022) by bulge type when estimating BH masses.

In our search for more subtle trends, we did not find any correlation between the Eddington ratio and offset from the $M_{\bullet} - \sigma_e$ relation, even after complementing our sample with the less-luminous RM AGN data. However, we cannot discount the possibility that the large uncertainties involved when estimating both the BH mass offset from $M_{\bullet} - \sigma_e$ and the Eddington ratio (~ 0.3 – 0.4 dex) may be washing out any potential weak correlation, further concealed by our small sample size. This is suggested in Figure 14 by the SDSS type 1 AGN data, which can be interpreted as a rough reference for the population of type 1 AGNs covering a representative range of Eddington ratios at low redshifts (Shen et al. 2008)^{9,10}. The SDSS data show an inverse correlation between the M_{\bullet} offset and $L_{\text{bol}}/L_{\text{Edd}}$ ($r = -0.31^{+0.05}_{-0.04}$, $p < 0.01$). It is worth noting that sample selection effects are also concerning. On the one hand, as discussed in Shen et al. (2008), an inverse correlation between $L_{\text{bol}}/L_{\text{Edd}}$ and the BH mass offset cannot be explained by the interdependence between L_{bol} , L_{Edd} , and M_{\bullet} , but it can be qualitatively produced if σ_e and $\lambda L_{\lambda}(5100 \text{ \AA})$ are positively correlated. We ascertain that this is the case for the AGN sample analyzed here ($r = 0.25^{+0.05}_{-0.05}$, $p = 0.03$). On the other hand, applying a luminosity threshold for selecting active galaxies, as was done for the PG quasars (Boroson & Green 1992) and CARS AGNs (Schulze et al. 2009), biases the samples toward AGNs with a high BH mass when considering the single-epoch virial mass estimate (Shen & Kelly 2010), making it harder to detect any residual correlation between the BH mass offset from

⁹ We only consider the σ_e estimates based on CaT modeling. The data were corrected by aperture effects; however, the bulge morphology was roughly approximated (see Shen et al. 2008, for more details).

¹⁰ The BH masses and Eddington ratios of the SDSS sample were updated following Ho & Kim (2015) for classical bulges.

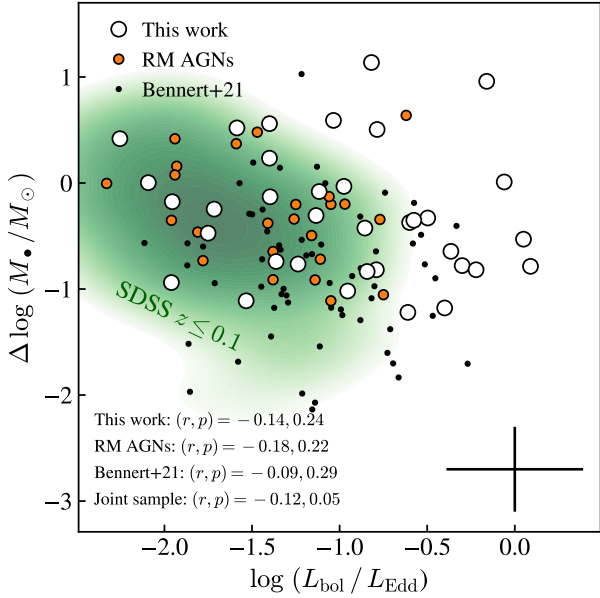


Fig. 14. Similar to Figure 12, but we add the RM AGNs presented in Ho & Kim (2014, 2015), the local AGN sample of Bennert et al. (2021), and the SDSS $z \leq 0.1$ type 1 AGNs provided by Shen et al. (2008).

$M_* - \sigma_e$ and the Eddington ratio. The effects of these potential confounding biases in producing the observed trend are, admittedly, uncertain.

There have been reports that AGNs with high $L_{\text{bol}}/L_{\text{Edd}}$ being systematically below the BH mass–host stellar mass relation (Volonteri et al. 2015; Shankar et al. 2019). Zhuang & Ho (2023) suggest that the level of BH accretion and star formation of an active galaxy is related to its position on the $M_* - M_*$ plane, with BH growth outpacing the host galaxy stellar growth when the BH is undermassive. They show that most of the local AGN hosts below the $M_* - M_*$ relation are late-type systems, with plenty of gas reservoirs as suggested by their blue color. We may be observing a similar trend in the $M_* - \sigma_e$ plane as well. If the BHs are growing more rapidly than the host galaxy bulges in local AGNs and quasars with a high Eddington ratio, then they may culminate on the $M_* - \sigma_e$ relation for classical bulges and ellipticals. Molina et al. (2023a) note that in the more gas-rich PG quasars, the BHs can increase their mass significantly while the bulges may have already finished their mass buildup, unless the host galaxies undergo merging. The amount of mass that BHs can accrete may be rooted at the given formation stage of the host galaxy central stellar spheroid (e.g., Merritt & Poon 2004; Miralda-Escudé & Kollmeier 2005; Anglés-Alcázar et al. 2017a), perhaps further modulated by a bursty nuclear stellar feedback episode (Anglés-Alcázar et al. 2017b), or self-limited by feedback from the central engine surrounding the BH (King 2010; King & Pounds 2015). Menci et al. (2023) suggest that the more efficiently accreting BHs tend to lie below the $M_* - \sigma_e$ for classical bulges and ellipticals due to the large gas fuel supply available within the host galaxies and the relatively weak AGN feedback in the high Eddington ratio regime. We can neither rule out nor probe this possibility, but we note that Molina et al. (2023b) report a weak correlation between the Eddington ratio and molecular gas fraction for $z \lesssim 0.5$ luminous AGNs, including the PG quasars and CARS AGNs.

To summarize, this study used archival MUSE observations for 42 local ($z \lesssim 0.1$) type 1 AGNs and quasars taken from the CARS and PG quasar surveys. Our main goal was to mea-

sure the bulge stellar velocity dispersion from the CaT stellar features and investigate the location of the host galaxies in the $M_* - \sigma_e$ relationship. We used annular apertures to extract the spectra and mitigate the effect of the AGN emission in diluting the host galaxy stellar features. Novel aperture corrections were developed to estimate accurate σ_e in these systems. Our main results are as follows:

1. The active galaxies have stellar velocity dispersion in the range $\sigma_* = 60\text{--}230 \text{ km s}^{-1}$. After correcting for aperture effects, bulge morphology, and observations' beam-smearing, we estimated σ_e values in the range $60\text{--}250 \text{ km s}^{-1}$.
2. By assuming a BH mass prescription that differentiates between classical bulges and pseudo bulges, we find that the CARS AGNs and PG quasars span over the $M_* - \sigma_e$ plane, with no statistical difference with respect to the inactive galaxies. The type 1 AGNs tend to preferentially follow the $M_* - \sigma_e$ relation of elliptical and classical bulges, with $\sim 25\%$ AGN host galaxies located in the $M_* - \sigma_e$ regime of pseudo bulges. We find two host galaxies above the local $M_* - \sigma_e$ relation, but systematics associated with galaxy morphology are likely hindering their σ_e estimates. If we do not differentiate by bulge type when estimating BH masses, the fraction of AGN hosts found below $M_* - \sigma_e$ mildly reduces to $\sim 16\%$, and the sample distribution AGNs on the $M_* - \sigma_e$ plane becomes inconsistent with that of the inactive galaxies.
3. We do not find any correlation between the BH mass offset from $M_* - \sigma_e$ and the Eddington ratio, even after complementing our sample with the less luminous reverberation-mapped AGNs and AGN host galaxies with spatially resolved σ_* profiles. However, we caution that this may be due to the large measurement uncertainties plus the small sample size.

Acknowledgements. We thank the anonymous referee for constructive comments and suggestions. LCH was supported by the National Science Foundation of China (11721303, 11991052, 12011540375, 12233001), the National Key R&D Program of China (2022YFF0503401), and the China Manned Space Project (CMS-CSST-2021-A04, CMS-CSST-2021-A06). K. K. acknowledges support from the Knut and Alice Wallenberg Foundation. This research has made use of the services of the ESO Science Archive Facility, and based on observations collected at the European Organization for Astronomical Research in the southern hemisphere under ESO programme IDs 094.B-0345(A), 095.B-0015(A), 097.B-0080(A), 099.B-0242(B), 099.B-0294(A), 0101.B-0368(B), 0103.B-0496(B) and 0104.B-0151(A), 106.21C7.002.

References

- Abolfathi, B., Aguado, D. S., Aguilar, G., et al. 2018, *ApJS*, **235**, 42
 Alexandroff, R., Strauss, M. A., Greene, J. E., et al. 2013, *MNRAS*, **435**, 3306
 Anglés-Alcázar, D., Davé, R., Faucher-Giguère, C.-A., Özel, F., & Hopkins, P. F. 2017a, *MNRAS*, **464**, 2840
 Anglés-Alcázar, D., Faucher-Giguère, C.-A., Quataert, E., et al. 2017b, *MNRAS*, **472**, L109
 Bacon, R., Conseil, S., Mary, D., et al. 2017, *A&A*, **608**, A1
 Baes, M., & Ciotti, L. 2019, *A&A*, **626**, A110
 Baes, M., & van Hese, E. 2011, *A&A*, **534**, A69
 Baringhaus, L., & Franz, C. 2004, *J. Multivar. Anal.*, **88**, 190
 Barth, A. J., Ho, L. C., & Sargent, W. L. W. 2002, *ApJ*, **566**, L13
 Beifiori, A., Maraston, C., Thomas, D., & Johansson, J. 2011, *A&A*, **531**, A109
 Bell, E. F., & de Jong, R. S. 2001, *ApJ*, **550**, 212
 Bennert, V. N., Auger, M. W., Treu, T., Woo, J.-H., & Malkan, M. A. 2011, *ApJ*, **726**, 59
 Bennert, V. N., Treu, T., Auger, M. W., et al. 2015, *ApJ*, **809**, 20
 Bennert, V. N., Loveland, D., Donohue, E., et al. 2018, *MNRAS*, **481**, 138
 Bennert, V. N., Treu, T., Ding, X., et al. 2021, *ApJ*, **921**, 36
 Bentz, M. C., & Manne-Nicholas, E. 2018, *ApJ*, **864**, 146
 Bentz, M. C., Denney, K. D., Grier, C. J., et al. 2013, *ApJ*, **767**, 149
 Bertram, T., Eckart, A., Fischer, S., et al. 2007, *A&A*, **470**, 571

- Bianchi, S., Guainazzi, M., Matt, G., Fonseca Bonilla, N., & Ponti, G. 2009, *A&A*, 495, 421
- Binney, J., & Tremaine, S. 2008, *Galactic Dynamics*, 2nd edn. (Princeton, NJ: Univ. Press)
- Blandford, R. D., & McKee, C. F. 1982, *ApJ*, 255, 419
- Bonning, E. W., Shields, G. A., Salviander, S., & McLure, R. J. 2005, *ApJ*, 626, 89
- Boroson, T. A., & Green, R. F. 1992, *ApJS*, 80, 109
- Bradley, L., Sipocz, B., Robitaille, T., et al. 2022, *astropy/photutils: 1.5.0, v1.5.0* (Zenodo), <http://dx.doi.org/10.5281/zenodo.596036>
- Busch, G., Smajić, S., Scharwächter, J., et al. 2015, *A&A*, 575, A128
- Caglar, T., Burtcher, L., Brandl, B., et al. 2020, *A&A*, 634, A114
- Cappellari, M. 2008, *MNRAS*, 390, 71
- Cappellari, M. 2016, *ARA&A*, 54, 597
- Cappellari, M. 2017, *MNRAS*, 466, 798
- Cappellari, M. 2023, *MNRAS*, 526, 3273
- Cappellari, M., & Emsellem, E. 2004, *PASP*, 116, 138
- Cappellari, M., Bacon, R., Bureau, M., et al. 2006, *MNRAS*, 366, 1126
- Croton, D. J., Springel, V., White, S. D. M., et al. 2006, *MNRAS*, 365, 11
- Dasyra, K. M., Tacconi, L. J., Davies, R. I., et al. 2007, *ApJ*, 657, 102
- de Nicola, S., Marconi, A., & Longo, G. 2019, *MNRAS*, 490, 600
- Ding, Y., Li, R., Ho, L. C., & Ricci, C. 2022, *ApJ*, 931, 77
- Dressler, A. 1984, *ApJ*, 286, 97
- Emsellem, E., Monnet, G., & Bacon, R. 1994, *A&A*, 285, 723
- Emsellem, E., Cappellari, M., Krajnović, D., et al. 2007, *MNRAS*, 379, 401
- Ferrarese, L., & Merritt, D. 2000, *ApJ*, 539, L9
- Ferrarese, L., Pogge, R. W., Peterson, B. M., et al. 2001, *ApJ*, 555, L79
- Fisher, D. B., & Drory, N. 2008, *AJ*, 136, 773
- Gao, H., & Ho, L. C. 2017, *ApJ*, 845, 114
- Gao, H., Ho, L. C., Barth, A. J., & Li, Z.-Y. 2020, *ApJS*, 247, 20
- Gebhardt, K., Bender, R., Bower, G., et al. 2000a, *ApJ*, 539, L13
- Gebhardt, K., Kormendy, J., Ho, L. C., et al. 2000b, *ApJ*, 543, L5
- Gravity Collaboration (Sturm, E., et al.) 2018, *Nature*, 563, 657
- Gravity Collaboration (Amorim, A., et al.) 2023, *A&A*, 669, A14
- Greene, J. E., & Ho, L. C. 2005a, *ApJ*, 627, 721
- Greene, J. E., & Ho, L. C. 2005b, *ApJ*, 630, 122
- Greene, J. E., & Ho, L. C. 2006a, *ApJ*, 641, 117
- Greene, J. E., & Ho, L. C. 2006b, *ApJ*, 641, L21
- Greene, J. E., Peng, C. Y., Kim, M., et al. 2010, *ApJ*, 721, 26
- Greene, J. E., Strader, J., & Ho, L. C. 2020, *ARA&A*, 58, 257
- Grier, C. J., Martini, P., Watson, L. C., et al. 2013, *ApJ*, 773, 90
- Guérou, A., Krajnović, D., Epinat, B., et al. 2017, *A&A*, 608, A5
- Gültekin, K., Richstone, D. O., Gebhardt, K., et al. 2009, *ApJ*, 698, 198
- Harris, C. E., Bennert, V. N., Auger, M. W., et al. 2012, *ApJS*, 201, 29
- Ho, L. C., & Kim, M. 2009, *ApJS*, 184, 398
- Ho, L. C., & Kim, M. 2014, *ApJ*, 789, 17
- Ho, L. C., & Kim, M. 2015, *ApJ*, 809, 123
- Hu, J. 2008, *MNRAS*, 386, 2242
- Hu, C., Li, S.-S., Yang, S., et al. 2021, *ApJS*, 253, 20
- Husemann, B., Singha, M., Scharwächter, J., et al. 2022, *A&A*, 659, A124
- Jarvis, M. E., Harrison, C. M., Mainieri, V., et al. 2020, *MNRAS*, 498, 1560
- Jørgensen, I., Franx, M., & Kjaergaard, P. 1995, *MNRAS*, 276, 1341
- Kaspi, S., Maoz, D., Netzer, H., et al. 2005, *ApJ*, 629, 61
- Kaspi, S., Brandt, W. N., Maoz, D., et al. 2021, *ApJ*, 915, 129
- Kellermann, K. I., Sramek, R. A., Schmidt, M., Shaffer, D. B., & Green, R. 1989, *AJ*, 98, 1195
- Kellermann, K. I., Sramek, R. A., Schmidt, M., Green, R. F., & Shaffer, D. B. 1994, *AJ*, 108, 1163
- Kim, M., & Ho, L. C. 2019, *ApJ*, 876, 35
- Kim, M., Ho, L. C., Peng, C. Y., et al. 2008, *ApJ*, 687, 767
- Kim, M., Ho, L. C., Peng, C. Y., Barth, A. J., & Im, M. 2017, *ApJS*, 232, 21
- King, A. R. 2010, *MNRAS*, 402, 1516
- King, A., & Pounds, K. 2015, *ARA&A*, 53, 115
- Kong, M., & Ho, L. C. 2018, *ApJ*, 859, 116
- König, S., Eckart, A., García-Marín, M., & Huchtmeier, W. K. 2009, *A&A*, 507, 757
- Kormendy, J., & Ho, L. C. 2013, *ARA&A*, 51, 511
- Kormendy, J., & Kennicutt, R. C., Jr 2004, *ARA&A*, 42, 603
- Kormendy, J., & Richstone, D. 1995, *ARA&A*, 33, 581
- Koss, M., Mushotzky, R., Veilleux, S., et al. 2011, *ApJ*, 739, 57
- Koss, M. J., Trakhtenbrot, B., Ricci, C., et al. 2022a, *ApJS*, 261, 1
- Koss, M. J., Trakhtenbrot, B., Ricci, C., et al. 2022b, *ApJS*, 261, 6
- Li, Y., Habouzit, M., Genel, S., et al. 2020, *ApJ*, 895, 102
- Lira, P., Kaspi, S., Netzer, H., et al. 2018, *ApJ*, 865, 56
- Liu, H.-Y., Liu, W.-J., Dong, X.-B., et al. 2019, *ApJS*, 243, 21
- López-Cobá, C., Sánchez, S. F., Anderson, J. P., et al. 2020, *AJ*, 159, 167
- Magorrian, J., Tremaine, S., Richstone, D., et al. 1998, *AJ*, 115, 2285
- Mathai, A. M., Saxena, R. K., & Haubold, H. J. 2009, *The H-Function*, 1st edn. (NY: Springer)
- Menci, N., Fiore, F., Shankar, F., Zanisi, L., & Feruglio, C. 2023, *A&A*, 674, A181
- Merritt, D., & Poon, M. Y. 2004, *ApJ*, 606, 788
- Miralda-Escudé, J., & Kollmeier, J. A. 2005, *ApJ*, 619, 30
- Moffat, A. F. J. 1969, *A&A*, 3, 455
- Molina, J., Wang, R., Shangguan, J., et al. 2021, *ApJ*, 908, 231
- Molina, J., Ho, L. C., Wang, R., et al. 2022, *ApJ*, 935, 72
- Molina, J., Ho, L. C., Wang, R., et al. 2023a, *ApJ*, 944, 30
- Molina, J., Shangguan, J., Wang, R., et al. 2023b, *ApJ*, 950, 60
- Nelson, C. H. 2000, *ApJ*, 544, L91
- Nelson, C. H., Green, R. F., Bower, G., Gebhardt, K., & Weistrop, D. 2004, *ApJ*, 615, 652
- Onken, C. A., Ferrarese, L., Merritt, D., et al. 2004, *ApJ*, 615, 645
- Persson, S. E. 1988, *ApJ*, 330, 751
- Peterson, B. M., Ferrarese, L., Gilbert, K. M., et al. 2004, *ApJ*, 613, 682
- Petric, A. O., Ho, L. C., Flagey, N. J. M., & Scoville, N. Z. 2015, *ApJS*, 219, 22
- Planck Collaboration XIII. 2016, *A&A*, 594, A13
- Quilley, L., & de Lapparent, V. 2023, *A&A*, 680, A49
- Reeves, J. N., & Turner, M. J. L. 2000, *MNRAS*, 316, 234
- Richards, G. T., Lacy, M., Storrie-Lombardi, L. J., et al. 2006, *ApJS*, 166, 470
- Saglia, R. P., Opitsch, M., Erwin, P., et al. 2016, *ApJ*, 818, 47
- Schaye, J., Crain, R. A., Bower, R. G., et al. 2015, *MNRAS*, 446, 521
- Schmidt, M., & Green, R. F. 1983, *ApJ*, 269, 352
- Schulze, A., Wisotzki, L., & Husemann, B. 2009, *A&A*, 507, 781
- Scott, N., van de Sande, J., Croom, S. M., et al. 2018, *MNRAS*, 481, 2299
- Sérsic, J. L. 1963, *Boletín de la Asociación Argentina de Astronomía La Plata Argentina*, 6, 41
- Shangguan, J., Ho, L. C., & Xie, Y. 2018, *ApJ*, 854, 158
- Shangguan, J., Ho, L. C., Bauer, F. E., Wang, R., & Treister, E. 2020a, *ApJ*, 899, 112
- Shangguan, J., Ho, L. C., Bauer, F. E., Wang, R., & Treister, E. 2020b, *ApJS*, 247, 15
- Shankar, F., Bernardi, M., Richardson, K., et al. 2019, *MNRAS*, 485, 1278
- Shen, Y., & Kelly, B. C. 2010, *ApJ*, 713, 41
- Shen, J., Vanden Berk, D. E., Schneider, D. P., & Hall, P. B. 2008, *AJ*, 135, 928
- Shen, Y., Greene, J. E., Ho, L. C., et al. 2015, *ApJ*, 805, 96
- Shi, Y., Rieke, G. H., Ogle, P. M., Su, K. Y. L., & Balog, Z. 2014, *ApJS*, 214, 23
- Shields, G. A., Gebhardt, K., Salviander, S., et al. 2003, *ApJ*, 583, 124
- Sijacki, D., Vogelsberger, M., Genel, S., et al. 2015, *MNRAS*, 452, 575
- Silpa, S., Kharb, P., Ho, L. C., et al. 2020, *MNRAS*, 499, 5826
- Silpa, S., Kharb, P., Ho, L. C., & Harrison, C. M. 2023, *ApJ*, 958, 47
- Smirnova-Pinchukova, I., Husemann, B., Davis, T. A., et al. 2022, *A&A*, 659, A125
- Soto, K. T., Lilly, S. J., Bacon, R., Richard, J., & Conseil, S. 2016, *MNRAS*, 458, 3210
- Thomas, N., Davé, R., Anglés-Alcázar, D., & Jarvis, M. 2019, *MNRAS*, 487, 5764
- Torbaniuk, O., Paolillo, M., Carrera, F., et al. 2021, *MNRAS*, 506, 2619
- Valdes, F., Gupta, R., Rose, J. A., Singh, H. P., & Bell, D. J. 2004, *ApJS*, 152, 251
- Vazdekis, A., Ricciardelli, E., Cenarro, A. J., et al. 2012, *MNRAS*, 424, 157
- Veilleux, S., Kim, D. C., Rupke, D. S. N., et al. 2009, *ApJ*, 701, 587
- Vestergaard, M., & Peterson, B. M. 2006, *ApJ*, 641, 689
- Volonteri, M., Silk, J., & Dubus, G. 2015, *ApJ*, 804, 148
- Volonteri, M., Dubois, Y., Pichon, C., & Devriendt, J. 2016, *MNRAS*, 460, 2979
- Watson, L. C., Martini, P., Dasyra, K. M., et al. 2008, *ApJ*, 682, L21
- Weilbacher, P. M., Palsa, R., Streicher, O., et al. 2020, *A&A*, 641, A28
- Wisotzki, L., Christlieb, N., Bade, N., et al. 2000, *A&A*, 358, 77
- Woo, J.-H., Treu, T., Barth, A. J., et al. 2010, *ApJ*, 716, 269
- Woo, J.-H., Schulze, A., Park, D., et al. 2013, *ApJ*, 772, 49
- Woo, J.-H., Wang, S., Rakshit, S., et al. 2024, *ApJ*, 962, 67
- Xie, Y., & Ho, L. C. 2022, *ApJ*, 925, 218
- Xie, Y., Ho, L. C., Zhuang, M.-Y., & Shangguan, J. 2021, *ApJ*, 910, 124
- Zhang, Z., Shi, Y., Rieke, G. H., et al. 2016, *ApJ*, 819, L27
- Zhao, Y., Ho, L. C., Shangguan, J., et al. 2021, *ApJ*, 911, 94
- Zhuang, M.-Y., & Ho, L. C. 2022, *ApJ*, 934, 130
- Zhuang, M.-Y., & Ho, L. C. 2023, *Nat. Astron.*, 7, 1376
- Zhuang, M.-Y., Ho, L. C., & Shangguan, J. 2018, *ApJ*, 862, 118

Appendix A: Additional material

Table A.1. Basic parameters of the sample.

Object	R.A. (J2000.0)	Decl. (J2000.0)	z	D_L (Mpc)	Morphology	$\log M_*$ (M_\odot)	$\log M_\bullet$ (M_\odot)	$\log \lambda L_\lambda(5100 \text{ \AA})$ (erg s^{-1})	R_e (")	n (kpc)	B/T	
(1)	(2)	(3)	(4)	(5)	(6)	(7)	(8)	(9)	(10)	(11)	(12)	
Palomar-Green Quasars												
PG 0050+124	00:53:34.94	+12:41:36.2	0.0611	282	Disk	11.12 ^{+0.3} _{-0.3}	7.57	44.76	1.33	1.62	1.7	0.52
PG 0923+129	09:26:03.29	+12:44:03.6	0.0287	131	Disk	10.71 ^{+0.3} _{-0.3}	7.52	43.83	1.01	0.60	1.0	0.37
PG 0934+013	09:37:01.05	+01:05:43.2	0.0506	230	Disk	10.38 ^{+0.3} _{-0.3}	7.15	43.85	0.57	0.58	0.5	0.05
PG 1011-040	10:14:20.69	-04:18:40.5	0.0584	268	Disk	10.87 ^{+0.3} _{-0.3}	7.43	44.23	0.84	0.98	2.8	0.14
PG 1126-041	11:29:16.66	-04:24:07.6	0.0601	278	Disk	10.85 ^{+0.3} _{-0.3}	7.87	44.36	0.66	0.79	4.0	0.37
PG 1211+143	12:11:17.67	+14:03:13.2	0.0815	400	Disk	10.38 ^{+0.3} _{-0.3}	8.10	45.04	0.95	1.51	5.8	0.72
PG 1244+026	12:46:35.25	+02:22:08.8	0.0484	220	Disk	10.19 ^{+0.3} _{-0.3}	6.62	43.77	0.10	0.10	1.0	0.03
PG 1426+015	14:29:06.57	+01:17:06.2	0.0866	401	Merger	11.05 ^{+0.3} _{-0.3}	9.15	44.85	0.98	1.64	4.0	1.0
PG 2130+099	21:32:27.81	+10:08:19.5	0.0631	292	Disk	10.85 ^{+0.3} _{-0.3}	8.04	44.54	2.26	2.83	4.0	0.33
CARS AGNs												
HE 0021-1810	00:23:39.34	-17:53:54.6	0.0537	247	Spheroidal	10.64 ^{+0.04} _{-0.05}	7.81	42.82
HE 0021-1819	00:23:55.29	-18:02:51.0	0.0533	245	Disk	10.50 ^{+0.04} _{-0.05}	7.10	42.80	1.9	2.04	1.4	0.33
HE 0040-1105	00:42:36.76	-10:49:22.4	0.0419	191	Spheroidal	10.16 ^{+0.13} _{-0.10}	7.43	43.13	0.9	0.77	3.5	0.5
HE 0108-4743	01:11:09.68	-47:27:35.6	0.0239	108	Disk	9.77 ^{+0.18} _{-0.10}	6.03	42.63	3.0	1.49	0.8	0.94
HE 0114-0015	01:17:03.51	+00:00:27.9	0.0458	210	Disk	10.47 ^{+0.13} _{-0.19}	6.78	42.64	2.8	2.60	0.3	0.97
HE 0119-0118	01:21:59.76	-01:02:24.4	0.0548	253	Disk	10.91 ^{+0.02} _{-0.06}	7.40	43.68	2.7	2.97	0.9	0.91
HE 0203-0031*	02:06:15.97	-00:17:28.9	0.0425	194	Peculiar	10.88 ^{+0.02} _{-0.01}	8.17	43.79	3.3	2.83	3.8	0.55
HE 0212-0059	02:14:33.58	-00:45:59.9	0.0264	119	Disk	10.59 ^{+0.01} _{-0.01}	8.18	43.33	1.2	0.66	0.7	1.0
HE 0224-2834	02:26:25.70	-28:20:59.2	0.0602	278	Peculiar	10.13 ^{+0.19} _{-0.17}	8.18	43.54	2.6	3.12	2.6	0.17
HE 0227-0913	02:30:05.51	-08:59:53.5	0.0165	74	Disk	9.92 ^{+0.17} _{-0.12}	6.27	43.15	0.7	0.24	1.0	0.96
HE 0232-0900	02:34:37.79	-08:47:15.5	0.0427	195	Peculiar	10.88 ^{+0.23} _{-0.12}	8.05	44.05	3.7	3.22	1.4	0.33
HE 0253-1641	02:56:02.70	-16:29:14.7	0.0319	145	Disk	10.28 ^{+0.11} _{-0.12}	6.64	43.16	3.3	2.17	0.9	0.80
HE 0345+0056	03:47:40.17	+01:05:14.8	0.0310	140	Spheroidal	8.85 ^{+0.62} _{-0.26}	6.92	43.97	1.3	0.83	2.0	0.06
HE 0351+0240	03:54:09.48	+02:49:31.3	0.0354	161	Peculiar	9.85 ^{+0.34} _{-0.70}	7.48	43.23	1.5	1.09	5.2	0.09
HE 0412-0803	04:14:52.65	-07:55:40.4	0.0380	173	Spheroidal	10.08 ^{+0.10} _{-0.12}	7.73	43.82	1.7	1.32	1.8	0.33
HE 0429-0247	04:31:37.12	-02:41:23.4	0.0423	193	Uncertain	9.18 ^{+0.51} _{-0.10}	6.61	43.35	0.9	0.78	0.7	0.86
HE 0433-1028	04:36:22.30	-10:22:33.1	0.0355	161	Disk	10.80 ^{+0.08} _{-0.09}	7.35	43.77	10.1	7.37	0.2	0.83
HE 0853+0102	08:55:54.25	+00:51:11.9	0.0526	241	Disk	10.54 ^{+0.04} _{-0.10}	7.25	42.99	0.9	1.07	0.8	0.86
HE 0949-0122	09:52:19.05	-01:36:43.7	0.0197	88	Spheroidal	10.02 ^{+0.09} _{-0.31}	6.58	42.72	1.5	0.62	3.5	0.05
HE 1017-0305	10:19:32.84	-03:20:14.6	0.0491	225	Disk	10.93 ^{+0.10} _{-0.15}	8.18	43.71	3.8	3.77	2.2	0.28
HE 1029-1831	10:31:57.33	-18:46:32.7	0.0405	185	Disk	10.49 ^{+0.06} _{-0.18}	7.06	43.30	2.1	1.74	0.7	0.50
HE 1107-0813	11:09:48.50	-08:30:14.7	0.0585	270	Disk	11.17 ^{+0.20} _{-0.38}	8.14	44.11	1.4	1.64	3.0	0.39
HE 1108-2813	11:10:47.99	-28:30:04.1	0.0240	108	Disk	10.29 ^{+0.11} _{-0.05}	7.06	43.04	5.8	2.90	0.2	0.99
HE 1237-0504	12:39:39.42	-05:20:38.5	0.0083	37	Disk	10.92 ^{+0.01} _{-0.01}	7.07	42.64	5.5	0.97	1.5	0.97
HE 1248-1356	12:51:32.39	-14:13:16.1	0.0145	65	Disk	10.31 ^{+0.01} _{-0.01}	6.58	41.93	1.1	0.34	1.5	0.99
HE 1330-1013	13:32:39.15	-10:28:52.4	0.0225	101	Disk	10.69 ^{+0.03} _{-0.13}	6.49	42.75	8.3	3.90	1.8	0.44
HE 1353-1917	13:56:36.77	-19:31:44.9	0.0348	158	Disk	10.99 ^{+0.03} _{-0.06}	8.20	43.10	11.4	8.16	2.7	0.01
HE 1417-0909	14:20:06.34	-09:23:12.8	0.0437	200	Disk	10.23 ^{+0.10} _{-0.17}	7.37	43.44	2.2	1.96	0.6	1.0
HE 2128-0221	21:30:49.96	-02:08:14.0	0.0527	242	Disk	9.93 ^{+0.21} _{-0.67}	6.71	43.02	2.1	2.23	1.7	0.01
HE 2211-3903	22:14:42.06	-38:48:22.7	0.0397	181	Disk	9.83 ^{+0.22} _{-0.21}	7.81	43.32	11.0	8.93	0.2	0.94
HE 2222-0026	22:24:35.22	-00:11:03.4	0.0581	268	Disk	10.20 ^{+0.09} _{-0.15}	7.28	43.41	1.1	1.28	1.1	0.50
HE 2233+0124	22:35:41.94	+01:39:34.5	0.0567	262	Disk	10.71 ^{+0.10} _{-0.03}	8.63	43.48	2.5	2.84	8.3	0.44
HE 2302-0857	23:04:43.70	-08:41:08.3	0.0470	215	Disk	11.20 ^{+0.09} _{-0.13}	8.54	43.93	3.9	3.72	5.5	0.39

Notes. (1) Source name. (2) Right ascension. (3) Declination. (4) Redshift. (5) Luminosity distance. (6) Morphological type of the host galaxy. For the PG quasars, we adopt the results of Kim et al. (2017), Zhang et al. (2016), and Zhao et al. (2021); for the CARS AGNs, we follow Husemann et al. (2022), but we relabel their “irregular” category to “peculiar” to avoid confusion with the “dwarf irregular” systems. We also relabel their “bulge-dominated” category to simply “spheroidal.” (7) Host galaxy stellar mass (Zhao et al. 2021; Smirnova-Pinchukova et al. 2022). (8) Black hole mass, based on the calibration of Ho & Kim (2015); the 1σ uncertainty is $\sim 0.32 - 0.38$ dex (Section 3.6). (9) AGN monochromatic luminosity at 5100 Å; for the CARS data, the values were derived from the broad H β luminosity following Greene & Ho (2005b). (10) Bulge effective radius. (11) Bulge Sérsic (1963) index. (12) Bulge-to-total (B/T) light fraction. The bulge properties for the PG quasars are obtained from optical and near-IR HST image modeling (Veilleux et al. 2009; Kim et al. 2017; Zhao et al. 2021), while for the CARS AGNs we adopt the MUSE-based i -band image models of Husemann et al. (2022), assuming the Sérsic model subcomponent with smaller R_e value. (*) For this target, the AGN optical spectrum and bulge properties were derived by Bennert et al. (2011) and Bennert et al. (2021), respectively.

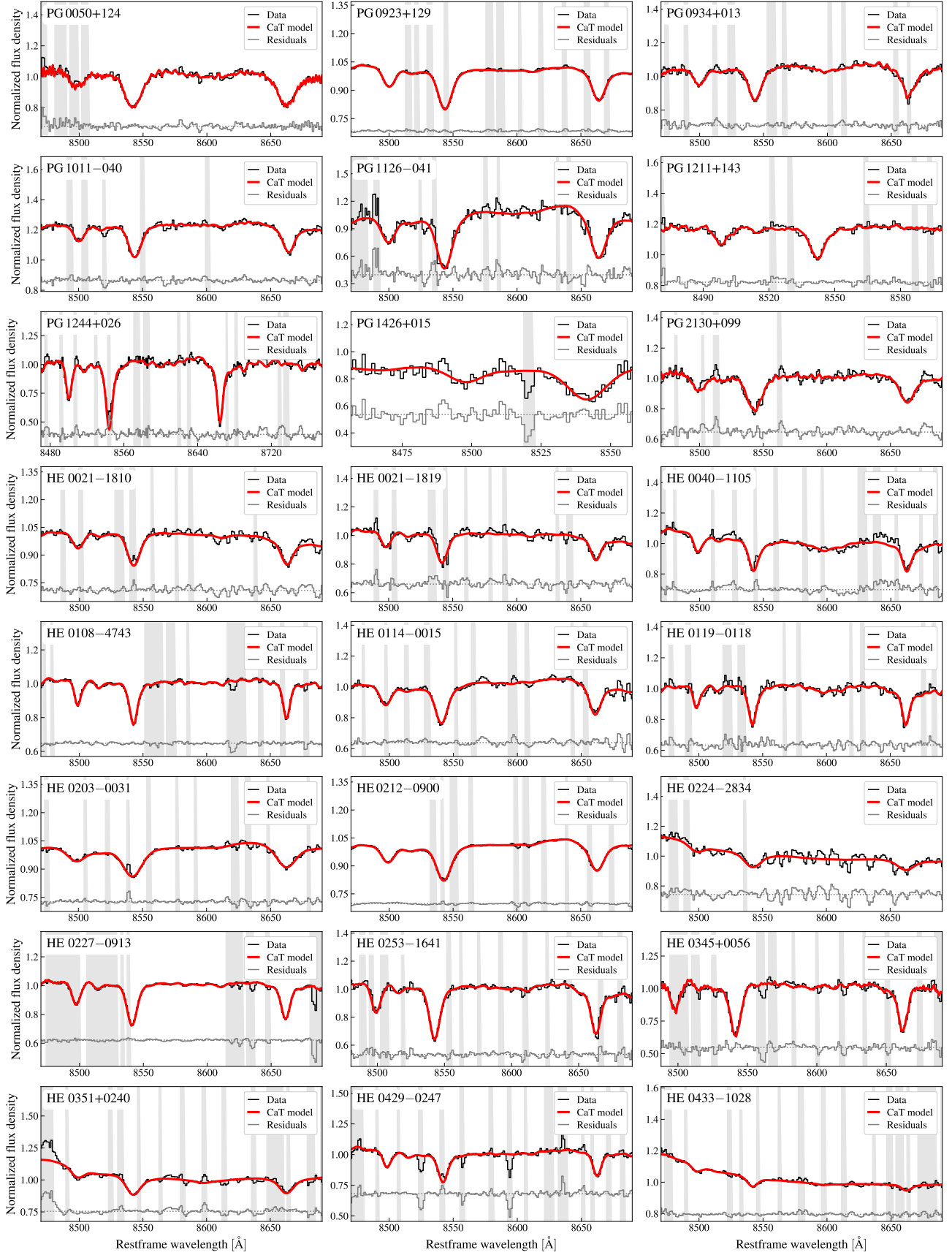


Fig. A.1. Extracted spectrum at the CaT wavelength range for each host galaxy. For clarity, the model residuals have been shifted to the flux density level indicated by the dotted line. The gray shaded regions represent the spectral windows that are masked to avoid prominent sky-line features detected in the corresponding variance spectra.

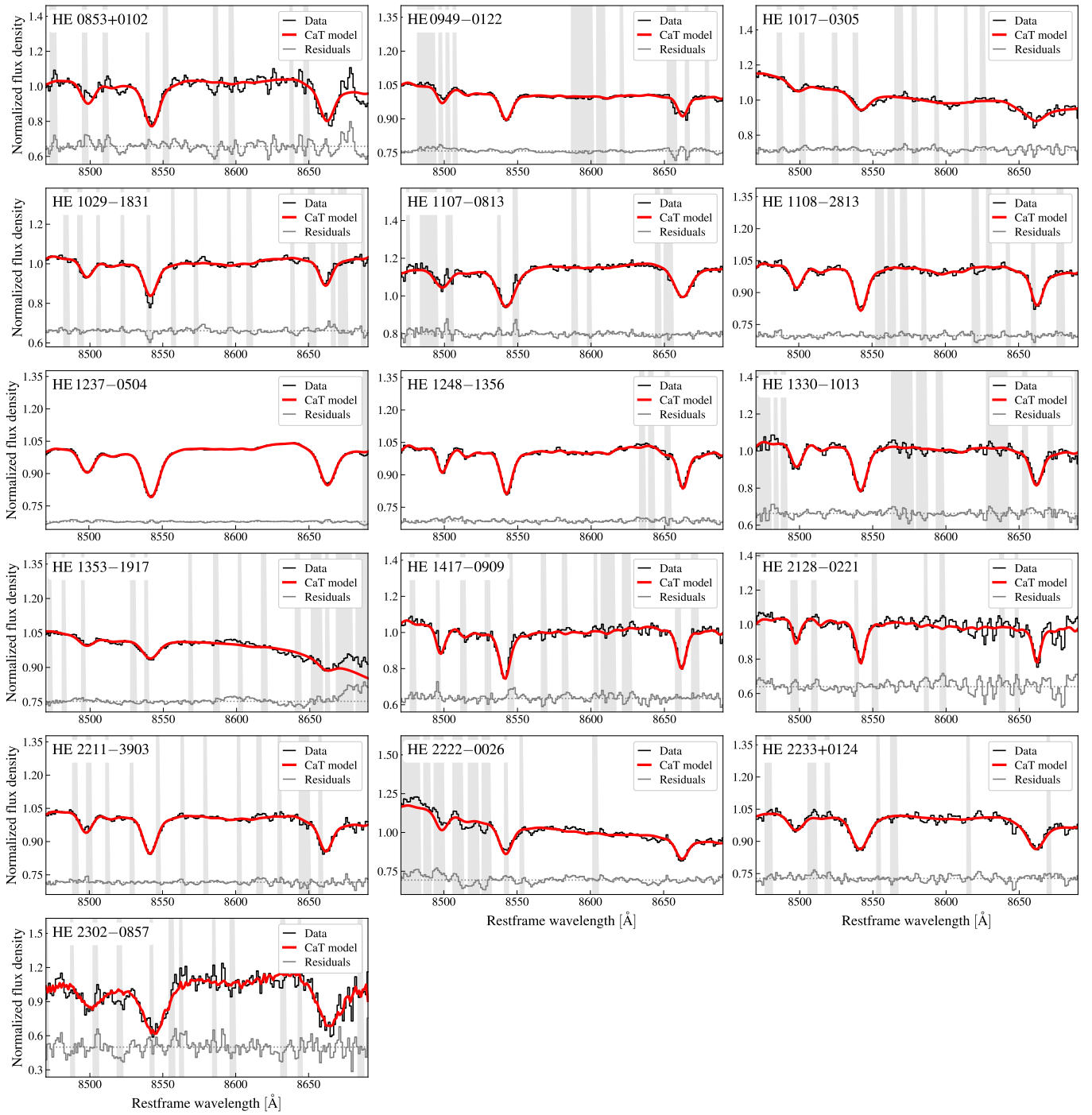


Fig. A.1. Continued.

Table A.2. MUSE observational setup.

Object	Observation Date	Exposure Time (s)	Image Quality (")	Instrument Mode
(1)	(2)	(3)	(4)	(5)
Palomar-Green Quasars				
PG 0050+124	06 Oct. 2019	9180	0.83	WFM-AO
PG 0923+129	28 Apr. 2019	2440	1.49	WFM-AO
PG 0934+013	04 Apr. 2015	1350	0.81	WFM-noAO
PG 1011-040	15 Jun. 2015	600	1.08	WFM-noAO
PG 1126-041	10 Sep. 2015	900	1.01	WFM-noAO
PG 1211+143	01 Apr. 2016	2800	0.76	WFM-noAO
PG 1244+026	30 May 2019	2440	1.08	WFM-AO
PG 1426+015	04 Apr. 2016	2800	0.60	WFM-noAO
PG 2130+099	25 Sep. 2019	2440	0.70	WFM-AO
CARS AGNs				
HE 0021-1810	19 Apr. 2016	1400	0.94	WFM-noAO
HE 0021-1819	19 Apr. 2016	1400	1.05	WFM-noAO
HE 0040-1105	19 Apr. 2016	800	1.41	WFM-noAO
HE 0108-4743	19 Apr. 2016	600	1.27	WFM-noAO
HE 0114-0015	12 Jul. 2016	900	0.66	WFM-noAO
HE 0119-0118	19 Apr. 2016	600	0.95	WFM-noAO
HE 0203-0031	27 Apr. 2016	800	1.12	WFM-noAO
HE 0212-0059	12 Dec. 2017	2200	0.95	WFM-noAO
HE 0224-2834	06 Jul. 2016	900	1.35	WFM-noAO
HE 0227-0913	27 Apr. 2016	1200	1.41	WFM-noAO
HE 0232-0900	19 Apr. 2016	600	1.03	WFM-noAO
HE 0253-1641	19 Apr. 2016	800	0.83	WFM-noAO
HE 0345+0056	19 Apr. 2016	1600	0.86	WFM-noAO
HE 0351+0240	19 Apr. 2016	1600	0.72	WFM-noAO
HE 0412-0803	19 Apr. 2016	1600	0.88	WFM-noAO
HE 0429-0247	19 Apr. 2016	2400	0.81	WFM-noAO
HE 0433-1028	19 Apr. 2016	600	0.55	WFM-noAO
HE 0853+0102	19 Apr. 2016	1200	0.57	WFM-noAO
HE 0949-0122	11 Mar. 2021	2300	1.16	WFM-noAO
HE 1017-0305	23 Jun. 2016	900	1.12	WFM-noAO
HE 1029-1831	19 Apr. 2016	600	0.66	WFM-noAO
HE 1107-0813	27 Jun. 2016	1350	0.90	WFM-noAO
HE 1108-2813	19 Apr. 2016	400	0.49	WFM-noAO
HE 1237-0504	24 May 2017	3600	0.52	WFM-noAO
HE 1248-1356	28 Jun. 2016	600	0.57	WFM-noAO
HE 1330-1013	20 Jun. 2016	600	0.67	WFM-noAO
HE 1353-1917	20 Jun. 2016	900	0.71	WFM-noAO
HE 1417-0909	20 Jun. 2016	1350	0.68	WFM-noAO
HE 2128-0221	25 May 2016	1350	0.68	WFM-noAO
HE 2211-3903	06 Jun. 2016	900	0.57	WFM-noAO
HE 2222-0026	20 Jun. 2016	1350	0.64	WFM-noAO
HE 2233+0124	23 Jun. 2016	1350	1.00	WFM-noAO
HE 2302-0857	09 Jun. 2016	600	0.66	WFM-noAO

Notes. (1) Source name. (2) Date of the MUSE observations. (3) Total exposure time. (4) Image quality of the observations as reported in the data cube header keyword "SKY_RES." (5) MUSE instrument mode. Most of the observations correspond to wide-field-mode natural-seeing (WFM-noAO), but four were aided by ground-layer adaptive optics (WFM-AO).

Appendix B: MUSE instrumental feature characterization

For each target, we characterize and correct the MUSE data for an instrumental feature seen at 9060–9180 Å in the observer frame. We derive an instrumental feature template from field stars that are also observed by MUSE. For each target, the annuli-extracted spectra are modeled using an instrumental feature template multiplied by a scaling factor plus a power-law continuum component. A template flux normalization is determined by calculating the average of the ratio between the template scaling factor and local spectrum continuum level across all

annular apertures. Figure B.1 shows the scaling factor as a function of the local continuum level for the PG quasar and CARS AGN samples. For all targets, the scaling factor is nearly proportional to the local continuum level, with minor variations corresponding to less accurate fits. By fitting a linear function to the data of each host galaxy, we recover slopes close to unity (as detailed for one case in Figure 3), in agreement with our supposition that the observed spectrum features are related to instrument response to incoming flux. The zero point variation among the sources indicates that the flux density normalization of the instrumental feature varies for each observation.

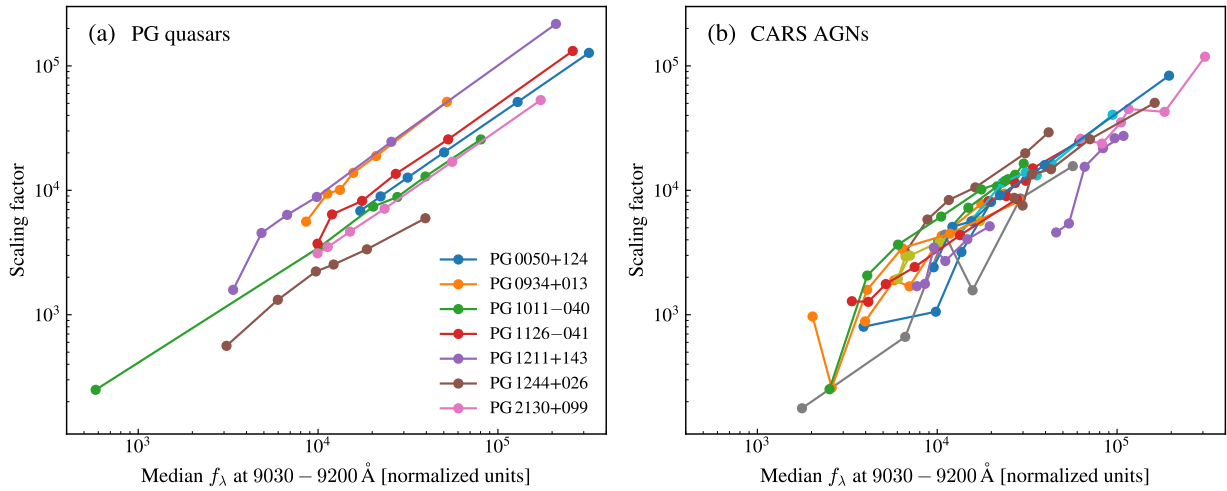


Fig. B.1. Scaling factor for the instrumental feature template as a function of the annuli-extracted spectra median flux density over 9030–9200 Å (observer frame) for (a) PG quasars and (b) CARS AGNs. The solid lines connect the data points corresponding to each observation.

Appendix C: Luminosity weighted σ_e

We estimate σ_e from a spectrum obtained by spatially collapsing the data cube over a given aperture. That is, we estimate σ_e from spatially unresolved data by adopting the convention of the SAURON/ATLAS^{3D} team (Emsellem et al. 2007)

$$G_e = \frac{\int_0^{R_e} I(R)G(R)R dR}{\int_0^{R_e} I(R)R dR}, \quad (\text{C.1})$$

where $I(R)$ is the surface brightness and G_e is the luminosity weighted mean of a quantity $G(R)$ within $1 R_e$. This approach differs from that commonly employed in M_* – σ_e relation studies, as these usually use spatially resolved observations to compute the luminosity weighted σ_e as follows (e.g., Gültekin et al. 2009)

$$\sigma_e^2 = \frac{\int_0^{R_e} (\sigma_V^2 + V^2)I(R) dR}{\int_0^{R_e} I(R) dR}, \quad (\text{C.2})$$

where V is the rotational component, and σ_V is the velocity dispersion. Kormendy & Ho (2013) show that both procedures provide consistent σ_e values for a local set of galaxies, independent of their bulge type (their Figure 11). In one of their tests, Bennert et al. (2015) show that their σ_e measurements are consistent with SDSS-based estimates, with the later based on aperture-extracted spectra.

Here, we test if both procedures used to estimate σ_e provide consistent results for mock data with properties similar to our sample. We model a galaxy as disk plus bulge, with each surface brightness component described by a Sérsic profile when projected on the sky. After setting the galaxy profile, we compute the second velocity moment map using JAMPY (Figure C.1 Cappellari 2008). We consider a PSF FWHM = 1". From this map, we estimate effective velocity dispersion within the bulge R_e following the common practice (σ_e^{2D} ; Gültekin et al. 2009). To build a three-dimensional data cube, we adopt a K-star spectrum template taken from the INDO-U.S. stellar spectral library of Valdes et al. (2004), and the two-dimensional surface brightness and kinematic maps for our galaxy model. The kinematic maps set the spectra Doppler shift and broadening at each data cube pixel that we must apply for. We convolve the spectra by the MUSE line spread function, accounting for the stellar template spectral resolution (FWHM = 1.35 Å; Beifiori et al. 2011). Finally, we collapse the data cube over a circular aperture equal to the bulge R_e to extract the spectrum and obtain the effective velocity dispersion (σ_e^{1D}). We repeat this process 500 times, varying the galaxy parameters randomly following uniform distributions with parameter ranges that encompass the observed values for our sample (Table A.1 and 1). Specifically, we consider galaxies with total mass between 9.6–11.2 M_\odot and bulge-to-total ratio in the 0.01–0.97 range. Sérsic index values in the 0.5–8 range for the bulge and 0.5–3 range for the disk. We set bulge effective radius in the range of 0.5–5", and the disk size can be 1.1–5 times larger. The bulge and disk can have different observed inclination on the sky. For both cases, the minor-to-major axis ratio range is 0.3–0.95, that is inclination angles between 0° (face-on) and 88° (edge-on). The axis ratio lower limit is set considering an intrinsic component axis-ratio of 0.2. Figure C.2 shows our test results. We find a good agreement between both estimates; the mean trend shows that σ_e^{1D} agrees with σ_e^{2D} by $\lesssim 10\%$ for $\sigma_e^{2D} \gtrsim 50 \text{ km s}^{-1}$. For $\sigma_e^{2D} \gtrsim 75 \text{ km s}^{-1}$, σ_e^{1D} overestimates σ_e^{2D} by merely $\sim 2\% \pm 2\%$. Such factor is

negligible considering the typical uncertainty of our measurements ($\sim 10\%$; Section 4.1). For $\sigma_e^{2D} \lesssim 50 \text{ km s}^{-1}$, we find that σ_e^{1D} increasingly overestimates σ_e^{2D} for lower values. However, both quantities remain closely correlated, with no significant dependence on the properties of the simulated systems. The overestimation of σ_e^{2D} by σ_e^{1D} for $\sigma_e^{2D} \lesssim 50 \text{ km s}^{-1}$ seems to be related to measuring velocity dispersion values close to or below the spectral resolution of the data (Scott et al. 2018), which is $\sim 36 \text{ km s}^{-1}$ for MUSE at 9000 Å (Guérou et al. 2017) and our mock data. Given the measured σ_* values for our sample (Table 1), this analysis suggests that we can safely compare our estimates with the spatially resolved σ_* measurements provided in the literature.

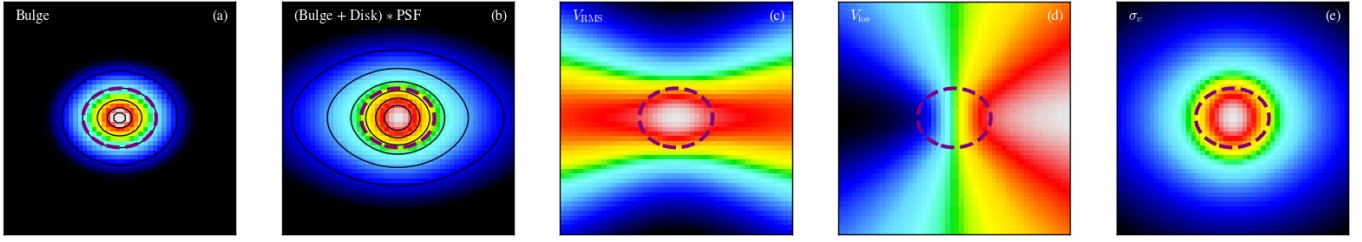


Fig. C.1. Example of a galaxy model analyzed in our test. (a) Intrinsic surface brightness distribution of the bulge. (b) Galaxy bulge plus disk surface brightness distribution convolved by PSF. (c) “RMS” velocity ($V_{\text{RMS}} \equiv \sqrt{\sigma_V^2 + V^2}$) map. (d) Line-of-sight velocity field. (e) Velocity dispersion map. In all panels, the magenta dashed curve shows the bulge half-light radius. We apply the color scale in panels (a) and (b). The galaxy kinematics obtained from JAMPY (Cappellari 2008).

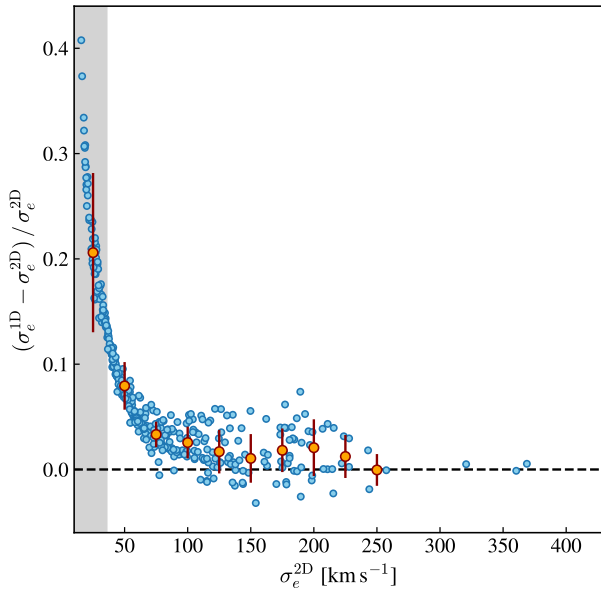


Fig. C.2. Relative difference between spatially resolved and aperture-based σ_e measurements. The orange circles represent the mean trend over 25 km s^{-1} -wide bins. The error bars correspond to the data scatter. The shaded region represents the spectrum resolution of MUSE in terms of line width ($\sim \text{FWHM}/2.355$).

Appendix D: Annular aperture correction factor

Aperture correction factors must be applied for estimating σ_e from projected (line-of-sight) second velocity moment (σ_{los}) measurements. We derive aperture correction factors under the assumption that the host galaxy bulge surface brightness emission on the sky is well-described by a Sérsic (1963) radial profile

$$I(R) = I_0 \exp(-b_n(R/R_e)^{1/n}), \quad (\text{D.1})$$

where I_0 is the central intensity and b_n is the constant that sets R_e as the half-light radius. By further assuming an isotropic velocity dispersion, σ_{los} can be calculated as (Baes & Ciotti 2019)

$$\sigma_{\text{los}}^2(R) = \frac{2}{I(R)} \int_R^\infty \frac{\nu(r)M(r) \sqrt{r^2 - R^2} dr}{r^2}, \quad (\text{D.2})$$

where $\nu(r)$ and $M(r)$ are the three-dimensional luminosity density and mass profiles, respectively. The $\nu(r)$ and $M(r)$ profiles are given by (Binney & Tremaine 2008)

$$\begin{aligned} \nu(r) &= \frac{-1}{\pi} \int_R^\infty \frac{dI(R)}{dR} \frac{dR}{\sqrt{r^2 - R^2}}, \\ M(r) &= 4\pi \left(\frac{M}{L}\right) \int_0^r \nu(r') r'^2 dr', \end{aligned} \quad (\text{D.3})$$

where M/L is the mass-to-light ratio, assumed to be constant in this work. The $\nu(r)$ and $M(r)$ profiles can be computed in terms of the Fox H function (Mathai et al. 2009) following Equations (17) and (25) of Baes & Ciotti (2019, see also Baes & van Hese 2011). For completeness, we also provide the formula for computing the projected (luminosity weighted) second velocity moment when adopting a circular aperture:

$$\sigma_{\text{los}}^2(<R) = \frac{\int_0^R I(R') \sigma_{\text{los}}^2(R') R' dR'}{\int_0^R I(R') R' dR'}. \quad (\text{D.4})$$

The PSF effect is considered following Emsellem et al. (1994, see also Cappellari 2008). We compute the PSF-convolved line-of-sight second velocity moment ($\tilde{\sigma}_{\text{los}}$) as

$$\tilde{\sigma}_{\text{los}}^2(R) = \frac{(I \sigma_{\text{los}}^2)(R) * \text{PSF}(R)}{I(R) * \text{PSF}(R)}, \quad (\text{D.5})$$

where the PSF follows a Moffat (1969) profile with $\beta \approx 2.2$ for MUSE data (Bacon et al. 2017; Guérou et al. 2017).

Figure D.1 shows the annular and circular aperture correction factors as a function of radius, normalized to R_e , and for different values of the Sérsic index n in the case of no PSF convolution. When using circular apertures, the correction factor is small ($\sim 10\%$), but non-negligible. The analytical formula accurately reproduces the empirical correction found by Cappellari et al. (2006) for local E/S0 galaxies. When considering annular apertures, the second velocity moment correction factor can be as high as 50%, depending on the Sérsic index and/or reasonable values for annular distance from R_e . Observing bulges with large Sérsic index (e.g., classical bulges) generally requires applying more significant corrections for σ_{los} to estimate σ_e at a fixed radius. Note that at large annular radii additional systematics could influence the estimation of σ_e (e.g., the kinematics of the disk). Figure D.1 highlights the difference between adopting annular and circular apertures for estimating σ_e and the importance of measuring σ_{los} as close as possible to R_e .

Figure D.2 shows the effect of PSF convolution on the recovery of σ_e . The overall effect is a decrease of the annular aperture correction factor that must be applied when the PSF FWHM increases relative to R_e , as expected due to the spreading of the central emission. This conclusion applies for values of Sérsic index beyond the $n = 1$ and 4 cases presented here. Figure D.3 presents the annular aperture correction factors as function of radius, normalized to R_e , for different Sérsic index n , and various ratios of $\xi \equiv \text{PSF FWHM}/R_e$. The annular aperture correction factor becomes less sensitive to the bulge Sérsic index for large ξ values, indicating that determining the underlying surface brightness profile is less critical.

Given that computing F_{ap} is considerably time intensive, we develop a cheaper numerical parameterization that can be used once the bulge profile and observation PSF have been characterized. The numerical parameterization is detailed in Equations 1 and 2, with input coefficients given in Table 2. These coefficients were derived by fitting F_{ap} in a radius range from 0.5 to $2.5 R_e$ in steps of $0.1 R_e$, $n = 0.5 - 8$ varying in bins 0.5 wide, and $\xi = 0 - 2.0$ sampled in steps of 0.25 . This numerical recipe is accurate up to 2%, sufficient given the larger uncertainties expected from modeling AGN host galaxy bulges. We note that, with the exception of the case of no PSF blurring ($\xi = 0$), our numerical recipe is only valid when the observation PSF is well-described by a Moffat profile. However, the procedure outlined here can be adopted for different representations of the PSF.

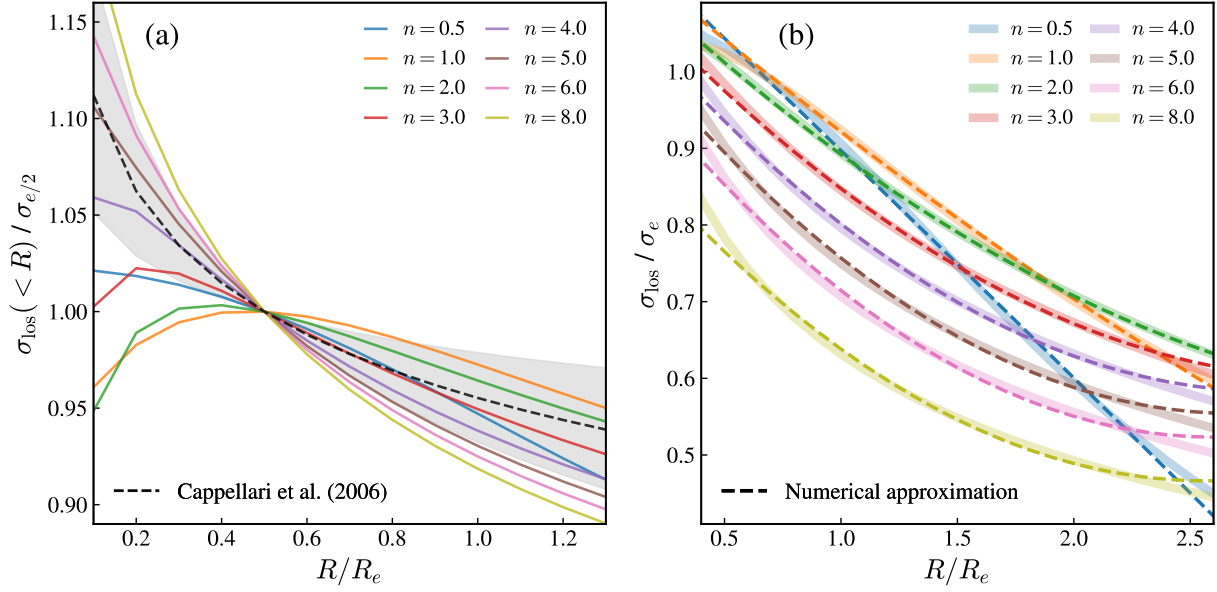


Fig. D.1. Aperture correction as a function of (a) the circular aperture size and (b) annular aperture location. The circular aperture correction values are normalized to the effective velocity dispersion at $R_e/2$ ($\sigma_{e/2}$), following Cappellari et al. (2006). We also highlight the empirical mean circular aperture correction provided by Cappellari et al. (2006) for local E/S0 galaxies, with the shaded region representing its scatter. The numerical approximation for the annular aperture correction factors corresponds to that of Equation 1, using the input coefficients presented in Table 2.

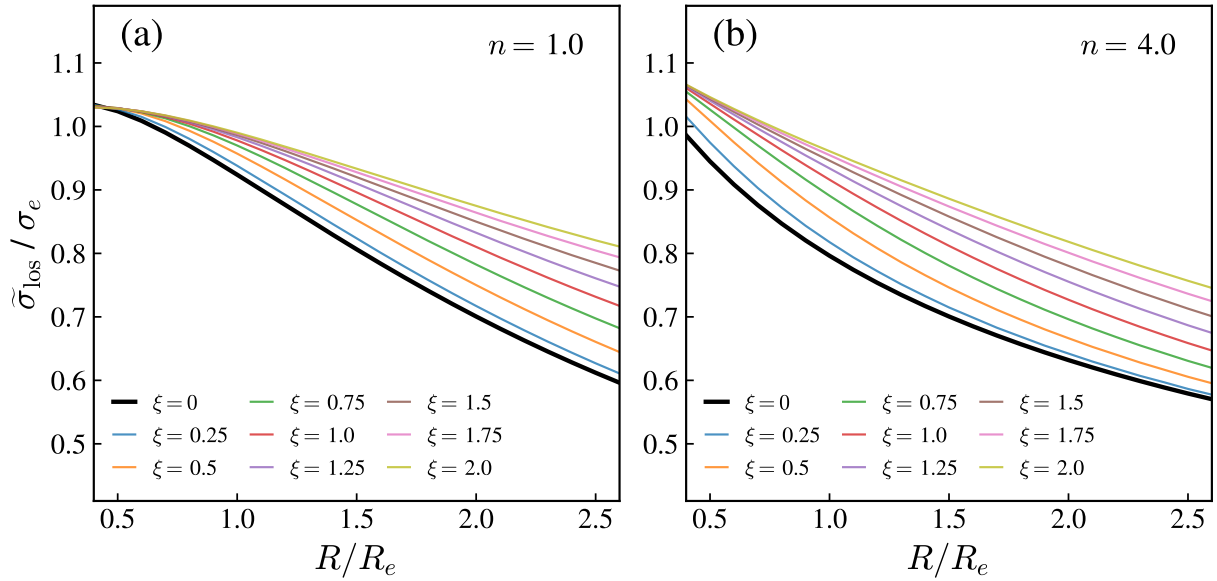


Fig. D.2. PSF convolution effect on the annular aperture correction factor for different values of PSF FWHM, normalized to Sérsic model R_e . We only show results for two Sérsic surface brightness profile cases (a) $n = 1$ and (b) $n = 4$.

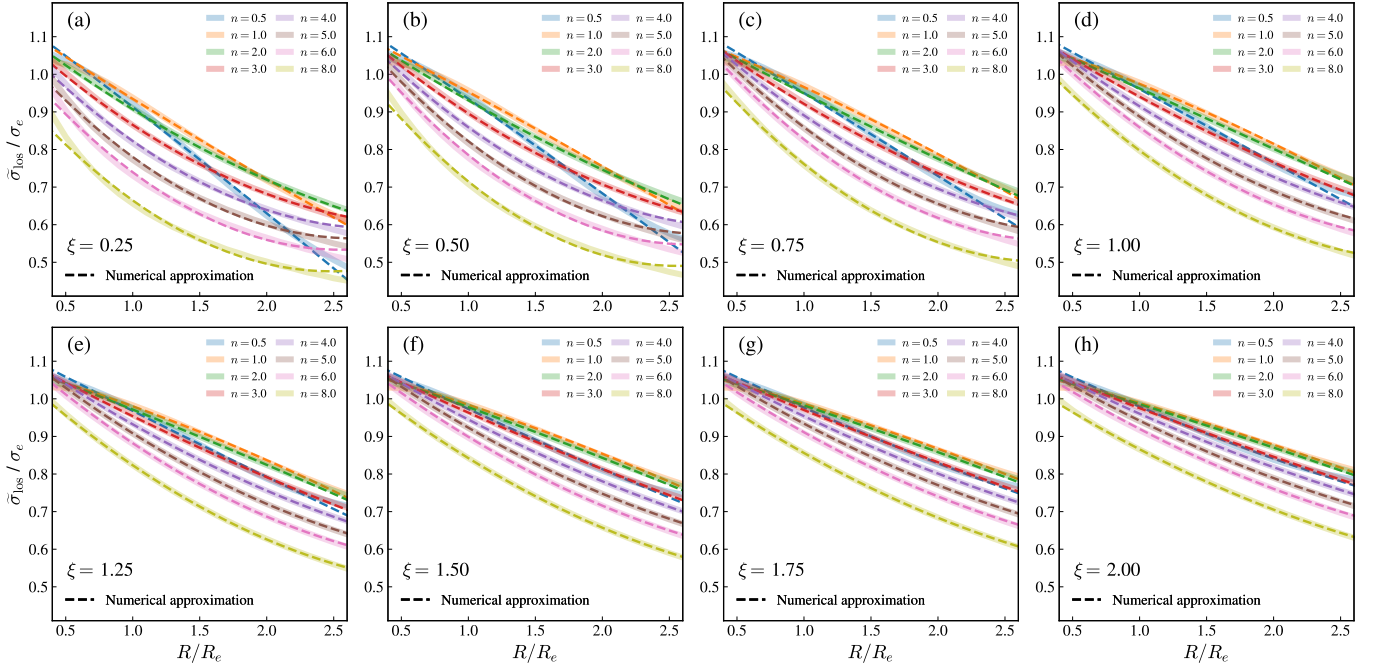


Fig. D.3. Annular aperture correction factor as a function aperture radial location. Panels (a) to (h) show particular cases of PSF FWHM values normalized to Sérsic model R_e . The numerical approximation for annular aperture correction factor corresponds to that of Equation 1, adopting the input coefficients presented in Table 2.